NUMERICAL SIMULATION OF VORTEX SHEDDING IN OSCILLATORY FLOWS

VIKAS KRISHNA

INFORMATION TO USERS

This manuscript has been reproduced from the microfilm master. UMI films the text directly from the original or copy submitted. Thus, some thesis and dissertation copies are in typewriter face, while others may be from any type of computer printer.

The quality of this reproduction is dependent upon the quality of the copy submitted. Broken or indistinct print, colored or poor quality illustrations and photographs, print bleedthrough, substandard margins, and improper alignment can adversely affect reproduction.

In the unlikely event that the author did not send UMI a complete manuscript and there are missing pages, these will be noted. Also, if unauthorized copyright material had to be removed, a note will indicate the deletion.

Oversize materials (e.g., maps, drawings, charts) are reproduced by sectioning the original, beginning at the upper left-hand corner and continuing from left to right in equal sections with small overlaps. Each original is also photographed in one exposure and is included in reduced form at the back of the book.

Photographs included in the original manuscript have been reproduced xerographically in this copy. Higher quality 6" x 9" black and white photographic prints are available for any photographs or illustrations appearing in this copy for an additional charge. Contact UMI directly to order.

UMI

A Bell & Howell Information Company
300 North Zeeb Road, Ann Arbor MI 48106-1346 USA
313/761-4700 800/521-0600

NUMERICAL SIMULATION OF VORTEX SHEDDING IN OSCILLATORY FLOWS

BY

©VIKAS KRISHNA, B.TECH.

A thesis submitted to the School of Graduate Studies
in partial fulfillment of the requirements for the degree of
Master of Engineering

Faculty of Engineering & Applied Science
Memorial University of Newfoundland

June, 1995

St. John's Newfoundland Canada

Abstract

Viscous forces that act on a body moving in a fluid may form a significant part of the total force acting on the body. The use of the linear potential-flow theory does not take into consideration the viscous effects that cause flow separation, skin-friction drag, and lift. Various methods have been developed and used to calculate the viscous forces numerically since Rosenhead's initial calculations. A review of the earlier work done in the area of vortex shedding and calculation of viscous flows is presented in chapter 1. Some vortex methods, that are commonly used, are described. One of these, the Discrete Vortex Method, is described in detail in chapter 2. This is demonstrated for a bluff body with sharp corners using the features of the Clement's model. However, this method does not simulate the effects of vorticity diffusion in the flow. Moreover, the body must also have sharp edges, which are taken to be the separation points.

Another method, that does not impose such limitations, is the Vortex-In-Cell(VIC) Method. This is developed and first applied to study flows past a circular cylinder in order to validate the method with existing results in chapter 3. Conformal transformations coupled with this method enable us to study flows past bodies of other cross-sectional shapes. Various mappings are derived and developed to simulate flows past a variety of shapes. A fin was added on to the body contour to simulate the effect of a skeg in the case of boat-sections. The force coefficients, C_D and C_M, were calculated at different Keulegan-Carpenter numbers and verified for sections like a circle, a flat plate, and a square, in an oscillatory flow, with the

results obtained by other workers. They were also calculated for a finned-circle, a section of a boat that is rounded and one that has hard chines. The theory and the method, the necessary modifications to the VIC method, and the simulation results are presented in chapter 4. A conclusion of the work done in the different chapters along with some comments are given in chapter 5.

I dedicate this thesis to my wonderful parents.

Prof.C.Bal Krishna

and Mrs. Sushila Krishna

Acknowledgments

I have received a great amount of support from an equally large number of people. Of all, I would first like to thank and express my deep gratitude to Dr. D.W.Bass, my supervisor, for his excellent guidance and support. In particular, I would like to acknowledge his suggestions at the crucial stages of this computational project. They showed me the way out of seemingly impossible situations.

I would also like to thank the Associate Dean of the Faculty of Engineering and Applied Science, Dr.J.J. Sharp, for his continued encouragement and support at various stages of the M.Eng. program. I also thank Dr. Bass, Dr. Sharp, and the School of Graduate Studies of Memorial University for the generous financial support, without which it would have been difficult to remain here and study.

Finally, I thank the staff of the Center for Computer Aided Engineering for their assistance and providing excellent computing services to the students of this faculty.

Contents

List of Figures

List of Symbols and Abbreviations

ω	: vorticity
$\tilde{\omega}$	: frequency of oscillatory flow
Γ	: circulation
δ	: Dirac delta
$\vec{r}$	: position vector
t	: time
$\hat{n}$	: unit normal
$\vec{u}$	: velocity vector
γ	: vorticity distribution function
σ_i	: core of vortex element
r_0	: outer radius of computational domain
ν	: kinematic viscosity
n_v	: number of newly created vortices
Δt	: time step
ψ	: stream function
k	: vortex strength
ρ	: fluid density
Re	: Reynolds number
KC	: Keulegan-Carpenter number
β	: Stokes parameter
C_D	: drag coefficient
C_M	: inertia coefficient

w	: complex potential
W	: complex velocity
F_P	: pressure force
F_f	: frictional force
J	: Jacobian of transformation
L	: characteristic length
β_f	: elongation factor
z	: physical plane
ζ	: computational plane

Chapter 1

Introduction

For the smooth and sound operation of marine vessels, such as ships and barges, the wave-induced roll motions must be accurately predicted. Calculations of the wave-exciting forces and the motions of vessels in waves can be made using the linear potential-flow theory. This, however, neglects viscous effects which cause flow separation and skin-friction drag. Also, for the linear theory to apply, the motions of the vessel and the wave amplitudes are assumed to be small in magnitude. Furthermore, the motions calculated using the linear theory are quite accurate for the degrees of freedom that are heavily damped but not for those that are lightly damped or for those where the damping is dominated by viscous effects and in particular for those with large amplitudes.

The main reason for this inaccuracy was the unavailability of good methods for determining the damping forces due to the viscous effects on the submerged body. The relative motion between the local fluid and the submerged vessel boundary causes flows which occur due to the unsteady boundary layer, its localized separations, and the associated vortex shedding especially near large changes in the curvature of the hull. Brown et al. [1] presented experimental evidence to show

that a major part of the viscous force acting on a barge with bluff right angle keel edges was due to vortex shedding. Work on this phenomenon has been carried out by many researchers using discrete-vortex-methods.

Vortex methods have been very widely used for simulating flows past bodies in order to determine the forces acting on them. Incompressible flows at high(> 500) Reynolds number are characterized by regions of concentrated vorticity. This vorticity in the flow is transported through the flow using the local velocity which in turn is calculated from the vorticity field. Poisson's equation for the stream function is solved to compute the local velocities to move the vorticity in the fluid. It becomes quite convenient to represent the flow in terms of regions of vorticity. Vortex methods are, therefore, employed to simulate flows by discretising the flow into regions of vorticity and then tracking this discretisation in a Lagrangian reference frame.

1.1 A Review

Rosenhead [2] was the first one to use a distribution of discrete vortices to represent a vortex sheet. His results were welcomed by other researchers and the method has been used since then till today. The most important part of Rosenhead's work was the numerical treatment of the Helmholtz instability phenomenon for longer durations. Helmholtz instability is the motion of adjacent portions of fluid of the same density with different speeds. The vortex sheet was replaced by a distribution of point vortices along its trace whose paths were determined by a numerical step-by-step method. At any instant of time, the line joining the positions of these vortices was assumed to be the approximate shape of the sheet at that time.

Rosenhead showed that the effect of the instability upon a surface of some form was to produce concentrations of vorticity at equal intervals along the surface and also that the surface of discontinuity tends to roll up around these points of concentration together with an accompanying increase in the amplitude of the displacement. He also attributed the approximate error, that crept in at each time step, to the truncation of the Taylor series for the displacement of the elemental vortices during each step. The method was not applicable to simulations involving longer durations as the errors introduced at each time step could get large enough to cause numerical difficulties.

The flow patterns that Rosenhead presented for Helmholtz instability were very realistic. As a result of this, his method of calculation was never really doubted. After 1959, criticism of his work was made by Birkhoff and Fisher [3], Hama and Burke [4], and others. It was pointed out that discrete vortices moving under their own influence in a two dimensional flow will always tend to a random distribution. Birkhoff and Fisher asserted that any decreases in distances between pairs of vortices would result in an increase for other pairs. They based this assertion on the theorem that the energy of a system of vortex filaments in a two-dimensional flow is constant. Since, for a system of vortices of equal strength, the energy is given by the product of all the initial distances, no two vortex lines can coalesce without an infinite increase in the separation of some other pair. Thus, according to them, the vorticity in a uniform array of point vortices can not become concentrated. They recalculated Rosenhead's results and found that the motion of the elemental vortices became very complicated in regions where some concentration took place, making it impossible to produce smooth vortex sheets.

Abernathy and Kronauer [5] explained the main features of the vortex street

formation mechanism from two initially parallel uniform vortex sheets of opposite sign. They found that no argument based solely on a linearized theory of disturbances can generate the asymmetry commonly associated with the interaction of the two sheets. They also used a numerical discretisation of the vortex sheets as Rosenhead did. Their non-linear method worked very well for a short time after the start of the flow but randomness appeared to creep into the calculations of the co-ordinates of the point vortices which eventually became so pronounced that it was said that, "there was no longer sufficient evidence to suggest the existence of vortex sheets". They concluded that clouds of vorticity have "a net strength diminished by the vorticity swept into the cloud by the opposite vortex row". Michalke [6] generalized the work of Rosenhead and of Abernathy and Kronauer by including the effect of the thickness of a shear layer. He represented the constant surface distribution of vorticity representing the initially linear velocity profile of the shear layer by a discrete number of surfaces of discontinuity, simulating each by a finite number of elemental vortices.

Further work was done to study vortex shedding from two-dimensional bodies. Modeling a flow around a sharp edge requires that the vorticity is shed from it in order to prevent infinite velocity at the edge. The shed vortices form a spiral which covers more and more area as vorticity is shed. According to the law of conservation of energy, this vorticity can not remain concentrated into a point and a core structure is formed. Anton [7] was the first one to model vortex shedding from a sharp edge using a semi-infinite plate in 1939. He found that the total vorticity shed is proportional to a one third power of time and that the distance from the edge to a point on the vortex sheet is proportional to the two thirds power of time. To determine the shape and the vorticity distribution of the sheet,

he divided the vortex sheet into an inner core and an outer loop linking it to the outer edge. The inner core was approximated by a spiral of the Kaden [8] type. Wedemeyer [9] recalculated Anton's results using a different method. However, neither Anton's nor Wedemeyer's solution is exact because of the over-simplified representation of the core region. But Wedemeyer's results are more complete. They provide useful information on the growth and distribution of vorticity and its total circulation. Anton's solution for the starting flow near a semi-infinite plate was then generalized by Blendermann [10]. He incorporated convex corners of any angle moving with velocity equal to the time raised to any power in a fluid at rest. These results were thought of as useful starting solutions in studying vortex shedding from more complicated boundaries in more general motions.

Other works in this area include those of Giesing [11], Clements [12], and Gerrard [13]. Giesing used non-linear representations for studying two-dimensional aerofoils in unsteady motion. Of importance is his discussion on the kinematics of vortex shedding. He claimed that the Kutta condition could be approximated by having a zero velocity difference at the trailing edges that are non-cusped. He showed that the error in the surface velocity distribution occurred only in the immediate neighbourhood of the edge.

Clements modeled the starting flow in the near wake of a bluff-based body. He brought forward some new features in the treatment of shedding conditions when only discrete elemental vortices are used. As the velocity at the shedding point could otherwise be infinite, Clements let the shed vortices start traveling with a velocity that is calculated a small distance away from the point of shedding. This avoided the need of a Kutta condition while maintaining a good amount of accuracy. He obtained some interesting results for the rate of shedding of vorticity

into the shear layer from two separation points, but these also are subject to the kind of criticism made of the Rosenhead model.

In 1967, Gerrard numerically calculated the magnitude and frequency of the lift force on a circular cylinder. He introduced a pair of elemental vortices into the flow some distance downstream at each time step to avoid the difficult problem of the determination of the separation points of the flow around a body without sharp edges. He used the shedding rate obtained experimentally to determine the strength of the vortices that are introduced at every time step. Even though the vortex positions looked quite irregular, the values of the lift force and the scale of formation regions were quite close to the experimental values for a range of Reynolds numbers.

Of interest to us is also the vortex separation that occurs from slender wings and bodies. Boundary layer separation takes place at the sides of aircraft wings and other slender bodies even at small angles of incidence. Coherent vortex sheets are formed and the study of these is of importance with respect to the non-linear lift, the roll-up of shed vorticity, etc., in the field of aeronautics; with respect to the non-linear force and moment in ship manoeuvrability, roll damping on bilge keels and fins, etc., in the area of ship hydrodynamics; and other areas in offshore engineering.

Roy and Legendre were the ones to make the major contributions in understanding the phenomenon of leading edge separation from slender wings in the early 1950's. However, the most successful and purely analytical model was developed by Brown and Michael [14] in 1954. Their results for the vortex positions, pressure distribution, etc. agreed only qualitatively with those obtained from experiments. However, their method has been used in many attempts to incorporate the effects

of non-conical planforms, thickness, and the unsteady motion for the calculation of stability derivatives. Other major numerical methods include Smith's iteration technique [15] and the multi-vortex model of Sack, Lundberg and Hanson [16]. Any models developed after these involved comparison with these two techniques, both of which were in moderate to good agreement with experiments. These techniques were also used by researchers to study vortex shedding from slender bodies alone and from a combination of a wing and a body. Smith's method is not easy to generalize for non-conical geometries, whereas Sack's method is. Sacks, Lundberg and Hanson used a Rosenhead discretisation in their model and obtained the kind of irregularity of the vortex sheets that is expected in applications of the Rosenhead method.

Ships can be considered as slender bodies. In a normal straight ahead course, boundary layer separation, which leads to the formation of coherent shear layers, occurs for most hull shapes. The vortex shedding that occurs is responsible for the non-linear force and moment met in ship manoeuvrability. Studying vortex shedding, using sections of ships, helps in investigating these effects and improving the geometry of the hull to minimize the adverse and unwanted forces. Hennig [17] used a single pair of discrete vortices to represent the non-linear side forces on slender ships with Lewis form cross-sections. Fuwa [18] refined Hennig's work by using a multi-vortex model for the bilge vortex separation on a ship which is being obliquely towed. Many writers have described the vortices produced at the bilges near the bows of ships. Tatinclaux [19] gave an approximate semi-empirical treatment of the corresponding increment in ship resistance or vortex drag. In 1971, Soh and Fink [20] modeled and studied vortex separation at the bilge keels of ships using potential flow. They presented a discrete vortex approximation for

the sheets using the Rosenhead method. They found that the use of constant time steps caused an early onset of breakdown of the calculations with crossing vortex sheets. Improvements were made by using varying time steps to ensure that the shedding point and the last two elemental vortices to be shed formed an equi-spaced set of points. A more thorough analysis led to the conclusion that the error is least when the elemental vortices are equi-spaced for the entire sheet at every instant for which the motion is calculated.

1.2 Common Vortex Methods

1.2.1 The Point Vortex Method

Rosenhead was the first one to attempt flow simulations using a vortex method in 1931. He approximated the motion of a two-dimensional vortex sheet by following the movement of a set of point vortices in time. The vorticity field, ω, was represented by

$$\omega(\vec{r}, t) = \sum_{i=1}^{N} \Gamma_i \delta(\vec{r} - \vec{r}_i(t)) \tag{1.1}$$

where δ is the Dirac delta function in two dimensions, $\vec{r}_i(t)$ is the location of the i^{th} vortex at an instant of time t, N is the total number of point vortices in the flow, and Γ_i, is the circulation of the i^{th} vortex. For a region $\Re$, the total circulation is given by

$$\Gamma_{\Re} = \int_{\Re} \vec{\omega}.\hat{n} ds \tag{1.2}$$

Here $\hat{n}$ is the normal to an elemental area, ds, of region $\Re$, and $\vec{\omega}$ is $\omega\hat{k}$. To satisfy the inviscid vorticity transport equation,

$$\frac{\partial \omega}{\partial t} + (\vec{u}.\nabla)\omega = 0, \tag{1.3}$$

or, in terms of the material derivative,

$$\frac{D\omega}{Dt} = 0. \tag{1.4}$$

the velocity of a vortex must be given by the value of the velocity field at the position of a vortex. Therefore,

$$\frac{d\vec{r_i}}{dt}(t) = \vec{u}(\vec{r_i}, t) \tag{1.5}$$

The velocity field, $\vec{u}(\vec{r}, t)$ is in turn determined from the solution of the Poisson equation

$$\nabla^2 \vec{u} = -\nabla \times (\omega \hat{k}) \tag{1.6}$$

The velocity field must satisfy the boundary condition of zero flow across the surface of the body. Therefore,

$$\vec{u}.\hat{n}|_{surface} = 0 \tag{1.7}$$

If the two-dimensional flow field has no interior boundaries and the fluid is at rest at infinity, the solution to equation 1.6 can be obtained from the Biot-Savart integral

$$\vec{u}(\vec{r}, t) = -\frac{1}{2\pi} \int_L \frac{(\vec{r} - \vec{r'}) \times \hat{k}\omega(\vec{r'}, t)}{\left|\vec{r} - \vec{r'}\right|^2} d\vec{r'} \tag{1.8}$$

where L is the length of the two dimensional vortex sheet. By substituting equation 1.1 in this formula, we can obtain $\vec{r_i}$ as the solution of the following system of non-linear ordinary differential equations:

$$\frac{d\vec{r_i}}{dt} = -\frac{1}{2\pi} \sum_{j=1, j\neq i}^{N} (\frac{(\vec{r_i} - \vec{r_j}) \times \hat{k}\Gamma_j}{|\vec{r_i} - \vec{r_j}|^2} \tag{1.9}$$

Rosenhead did all the calculations by hand. With the advent of computers, more accurate results were attempted as more point vortices could be used. However, using a larger number of point vortices of lower strengths did not yield a convergent solution. In many simulations, the motions of the vortices became quite chaotic. Therefore, although the point vortex method solves the Euler equations, a system of point vortices does not represent a vorticity field very well. Better results with this method were obtained using fewer vortices together with a diffusive time integration scheme.

1.2.2 The Vortex Blob Method

One of the other methods for simulating two-dimensional flows is the vortex blob method. In this method, vortices with finite cores, or vortex blobs, are used as the computational elements. The equation for the representation of the vorticity field now becomes

$$\omega(\vec{r}, t) = \sum_{i=1}^{N} \Gamma_i \gamma_i[\vec{r} - \vec{r_i}(t)] \tag{1.10}$$

where γ_i is the vorticity distribution within the vortex located at $\vec{r_i}$ with the normalization

$$\int_C \gamma_i(\vec{r}) d\vec{r} = 1 \tag{1.11}$$

where C is the core boundary. We assume that

$$\gamma_i(\vec{r} - \vec{r_i}) = (1/\sigma_i^2) f(|\vec{r} - \vec{r_i}| / \sigma i) \tag{1.12}$$

where f is a distribution function whose shape is common to all vortex elements and σ_i is referred to as the core of the vortex element i. For example, if the vorticity

distribution is given by the Gaussian distribution such that

$$\gamma_i(\vec{r}) = \frac{1}{\pi\sigma_i^2} exp(-|\vec{r}|^2/\sigma_i^2) \tag{1.13}$$

then the distribution function $f(\vec{r})$ is given by

$$f(|\vec{r} - \vec{r_i}|/\sigma i) = \frac{1}{\pi} exp(-|\vec{r} - \vec{r_i}|^2/\sigma_i^2) \tag{1.14}$$

This function satisfies the viscous part of the vorticity transport equation

$$\frac{D\omega}{Dt} = \nu\nabla^2\omega \tag{1.15}$$

The velocity induced by the vorticity field, equation 1.10, is given by

$$\vec{u}(\vec{r}, t) = -\frac{1}{2\pi}\sum_{j=1}^{N} \frac{(\vec{r} - \vec{r_j}) \times \hat{k}\Gamma_j g(|\vec{r} - \vec{r_j}|/\sigma_j)}{|\vec{r} - \vec{r_j}|^2} \qquad r \neq r_j \tag{1.16}$$

where g is given by

$$g(y) = 2\pi\int_0^y f(z)zdz \tag{1.17}$$

The use of distributed vortex cores or vortex blobs yields more realistic vorticity distributions and bounded induced velocities for all the vortex elements. As per equation 1.16, the velocity of the vortex blobs is given by

$$\frac{d\vec{r_i}}{dt} = \vec{u}(\vec{r_i}, t) = -\frac{1}{2\pi}\sum_{j=1, i\neq j}^{N} \frac{(\vec{r_i} - \vec{r_j}) \times \hat{k}\Gamma_j g(|\vec{r_i} - \vec{r_j}|/\sigma_j)}{|\vec{r_i} - \vec{r_j}|^2} \tag{1.18}$$

which is actually the velocity field at the center of the blob.

In contrast to the point vortex method, an error in the spatial accuracy arises in the vortex blob method because the computational elements are assumed to retain their shapes throughout the simulation, whereas a real fluid with vorticity may suffer a considerable amount of strain. Hald and Del Prete [21] studied the

convergence of this method to the solution of the Euler equation and showed that convergence occurred only for a limited time interval with an error that grew exponentially in time.

The use of the vorticity diffusion term, $\nu\nabla^2\omega$, in the vorticity transport equation has two important consequences. They are, firstly the vorticity creation at the boundary and secondly the diffusion of the vorticity in the flow field. The diffusion of vorticity can be simulated either by allowing the vortex cores to increase in size or, as proposed by Chorin [22], adding a random walk to the position of the vortices at each time step. However, Greengrad [24] pointed out that in the core spreading technique, the vorticity is correctly diffused but incorrectly convected. Therefore, this technique is inaccurate and converges to a system of equations different from the Navier-Stokes equations. Chorin's random vortex method, on the other hand, is a correct approximation. The random walk step length used here is proportional to $(\nu\Delta t)^{1/2}$, the idea being that the effects of viscosity be reproduced correctly in a statistical sense. It was pointed out that in the case of flows past bluff bodies, where the boundary-layer separation is an important physical phenomenon, the creation of vorticity at the body contour and its transportation along the body surface must be modeled correctly. Many workers introduced circulation at the separation points that were determined using boundary-layer calculations, experimental information, etc. They determined the rate of creation of vorticity from the kinematic condition

$$\frac{d\Gamma}{dt} = -\frac{1}{2}(u_+^2 - u_-^2) \tag{1.19}$$

where $u_\pm$ are the upper and lower speeds on the sides of the separating shear layer and $(d\Gamma/dt)$ is the rate of change of circulation in the shear layer.

Another approach to the creation of vorticity is to introduce vortices at the boundary to satisfy the no-slip condition at the surface. Chorin employed this approach and presented a scheme that converged to the solution of the Navier-Stokes equations. The three steps in his scheme were the creation of vortices at the boundary to maintain the no-slip condition at the surface, move all the vortices with local velocities to take-care of the inviscid part of the equations of motion, and finally the diffusion of the vorticity simulated by a change in the core size, σ, or adding a random walk to the position of the vortices.

In both the point vortex and the vortex blob method, the computational elements are moved with velocities that are calculated using a Green's function solution to the Poisson equation. If N such elements are used to simulate the flow, then the number of operations required to compute all the velocities is of the order of N^2. This is quite costly in terms of the computational time that a computer spends simulating a flow. However, there are ways round this problem and the computational time can be brought down by combining a number of elements in a given region into a representative computational element. This gives rise to a different class of methods for simulating flows, called the Vortex-In-Cell methods. Another way, in which the number of computational operations can be reduced, is that employed by Yeung et al. [25]. They used the fast adaptive multipole algorithm for particle simulations of Carrier et al. [26] which reduces the computational effort to the order of N.

1.2.3 The Vortex-In-Cell Method

In this method, a mixed Eulerian-Lagrangian approach is used. The Lagrangian treatment of the vorticity is retained and the Poisson equation for the velocity

field is solved in a fixed Eulerian mesh. As compared to the previous two methods where the operation count was of the order of N^2, where N was the number of computational elements used, the operation count here is of the order of $MlogM$ where M is the total number of grid points in the mesh. An additional number of steps of the order of N that are required are for the generation of the mesh values for the vorticity from the Lagrangian representation and the interpolation of the velocities from the mesh back into the Lagrangian points. The number of mesh points, M, depends on the problem to be solved.

Every element, i.e. every vortex, lies in a particular cell of the mesh. Its circulation is distributed onto each of the four corners(nodes) of that cell according to the area weighting scheme

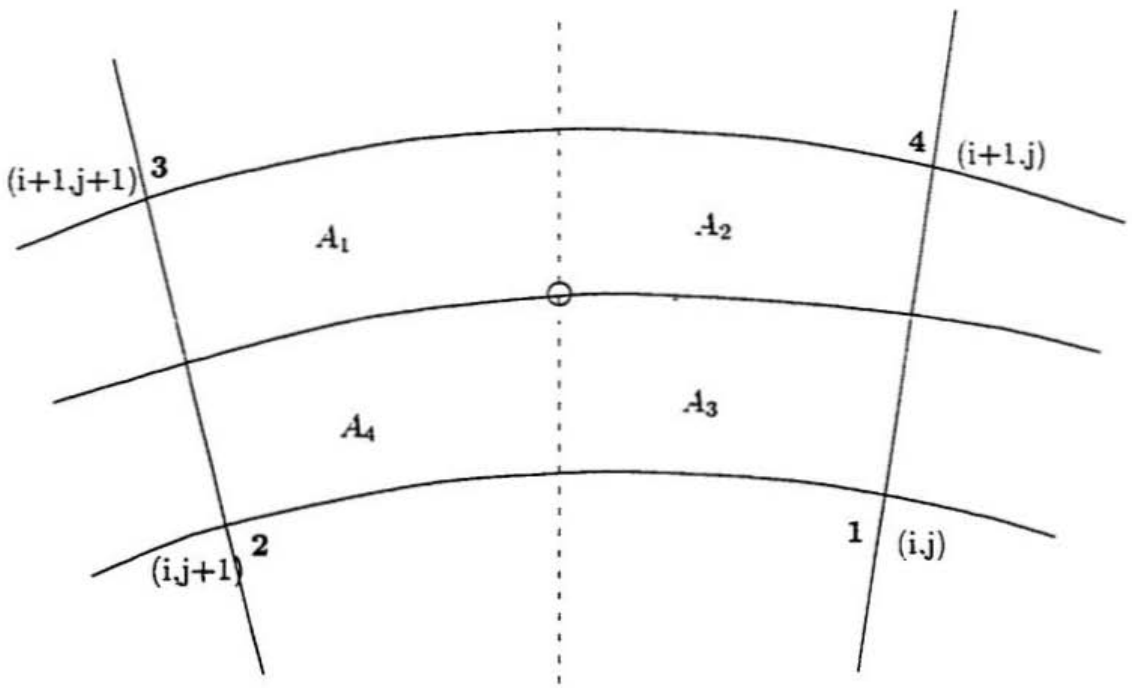

Figure 1.1: Area Weighting Scheme.

$$\Gamma_{node_k} = \frac{\Gamma_{vortex} A_k}{A_T} \tag{1.20}$$

where Γ_{vortex} is the circulation of the vortex and $A_T = \sum_{k=1}^{4} A_k$, A_k being the area of a region as shown in figure 1.1. The Poisson equation for the stream function, ψ,

$$\nabla^2 \psi = -\omega \tag{1.21}$$

is then solved. Once the stream function is known at all of the mesh points, then the velocities at the mesh points can be computed using the central difference method for example.

$$u_{i,j} = \frac{\psi_{i,j+1} - \psi_{i,j-1}}{2h} \tag{1.22}$$

$$v_{i,j} = -\frac{\psi_{i+1,j} - \psi_{i-1,j}}{2h} \tag{1.23}$$

where h is the mesh spacing. Once again, the area weighting scheme is employed to determine the velocity of a vortex that is contained in a cell of the mesh as given by

$$\vec{u}_{vortex} = \sum_{k=1}^{4} \frac{\vec{u}_k A_k}{A_T} \tag{1.24}$$

As can be seen from these formulae, the vorticity distribution onto the mesh and the interpolation of the nodal velocities requires a fixed number of operations per vortex giving an operation count of the order of N per time step. Christiansen [27] and Baker [28] used the VIC method and reported some interesting results. Christiansen, for example, showed that the vortices that have the same circulation pre-

cess about each other. With time, they either coalesce or they do not depending on their initial separation.

The VIC method also suffers from numerical errors as do other methods. In addition to the errors that come up in the vortex blob method, the distribution of the vorticity onto the mesh nodes and the interpolation of the nodal velocities to obtain vortex velocities have errors associated with them. Errors also creep in due to the differencing procedures used to solve the Poisson equation to determine the mesh velocities. However, results of numerical experiments in two dimensions have indicated that these errors do not seriously affect the large-scale features. Hockney et al. [29] proposed an improvement to the VIC method. They suggested using nine surrounding nodes to distribute the vorticity onto and using their nine nodal values of the velocity to interpolate for the calculation of the velocity of a vortex, instead of using the nearest surrounding four nodes only. They state that the mesh errors are reduced by two orders of magnitude by this technique.

This method is further explained in full detail in chapter 3. It is validated using existing results for the flow past a circular cylinder. Numerical experiments for bodies other than a circular cylinder were carried out using this method coupled with conformal transformations. The results are presented in chapter 4.

1.3 Summary

For incompressible flows, knowledge of the vorticity distribution allows us to determine the velocity field. Vorticity moves with the local velocity in the inviscid motion of a fluid. Vortex methods present a numerical algorithm for flow simulation based on these facts. They offer a number of advantages over the Eulerian

schemes. But every advantage has a drawback associated with it. The user of a particular method has to make a judicious choice of a method exploiting the advantages and employing means to circumvent the disadvantages of a particular method. Some of these are worth mentioning once again.

Vortex methods require only a small number of storage locations because computational elements are required only in the rotational parts of the flow. The associated disadvantage is that the number of operations per time step is proportional to the square of the number of vortex elements or coordinates in the discretisation. This leads to a rapid increase in the computation time as the number of computational elements is increased. The boundary condition at infinity can be satisfied very accurately, whereas the no-slip condition at the body surface requires some care. In the case of turbulent flows and laminar flows at high Reynolds numbers, fine-scale structures may develop in an intermittent manner throughout the flow field. Vortex methods allow such regions to develop by a local concentration of computational elements. This however leads to the requirement of remeshing which, in turn, gives rise to other numerical difficulties and approximations. However, the advantages of the vortex methods have made them popular for simulating flows. Many workers have proposed improvements to minimize their disadvantages and they are still being used and worked on.

Chapter 2

Point Vortex Method(Clements)

In this study, a model for the two dimensional inviscid flow near the wake of a bluff body is constructed. This model is used in studies of vortex shedding from bodies with well defined separation points(sharp edges), such as keels, wings, and fins. The applications of the method include manœvring of crafts, roll-damping of ships, etc. Discrete point vortices are used for the representation of the continuous vortex sheets. As the model is based on inviscid flow, it does not take care of the possible diffusion of vorticity in the flow. Therefore, it can not be used to study flows that are significantly affected by viscous diffusion mechanisms(for example flows at low Reynolds numbers). The bluff body used here has sharp corners, and thus, fixed separation points. Such a shape is chosen to obviate the need for any assumptions of the position of the separation points.

2.1 The Model

The bluff body is a plane-based two dimensional body with right angles between the sides and the rear face. The flow is assumed to separate at the corners of

the body and remain attached on the side faces. The shear layers shed from the corners, i.e., the separation points, are approximated by arrays of line vortices. The velocity of a particular vortex in the flow is calculated by adding the two dimensional irrotational potential flow around the body and the velocity induced at the position of that vortex by all the other vortices present in the flow. To obtain these velocities, a Schwartz-Christoffel transformation is used to project the exterior region of the body, which is assumed to extend to infinity upstream, into an upper half plane with the boundary of the body mapped along the real axis. This transformation, given by,

$$z = -(2is/\pi)[sin^{-1}(\lambda) + \lambda(1-\lambda^2)^{1/2}] \tag{2.1}$$

or

$$z = (2is/\pi)\{iln[i\lambda + (1-\lambda^2)^{1/2}] - \lambda(1-\lambda^2)^{1/2}\} \tag{2.2}$$

transforms the rear corners of the body $z = \pm is$ into the points $\lambda = \mp 1$ as shown in figures 2.1 and 2.2. The irrotational flow used has two components. They are shown in figure 2.3. The first component is a flow with velocity $(U_0, 0)$ far upstream and downstream and the second has a velocity $(0, -pU_0)$ at $z = 0$ and $|\vec{u}| \to 0$ as $|\vec{z}| \to \infty$. This is a circulatory flow in the region of the base and is used to create the initial asymmetric disturbance when the flow is started from rest. Hence p was taken to be $0.1sin(\frac{\pi t}{3})$ for $t < 3$ and zero for $t \geq 3$. The flow starts impulsively from rest and initially develops symmetrically. The introduction of a small asymmetric disturbance results in an asymmetric interaction of the shear layers which amplifies into steady vortex-shedding motion.

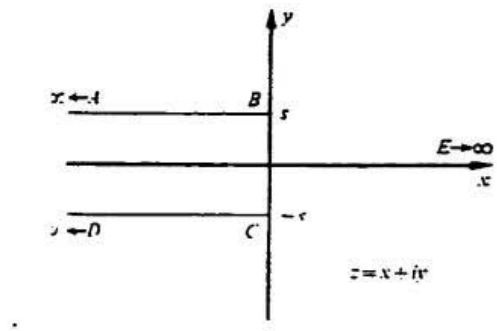

Figure 2.1: The physical z-plane.

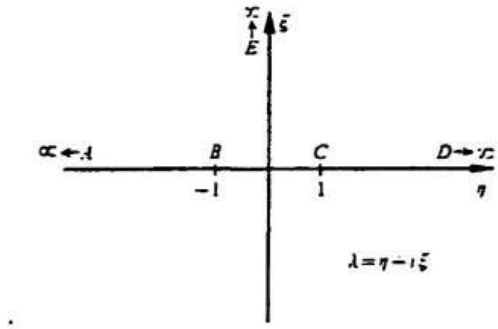

Figure 2.2: The transformed λ-plane.

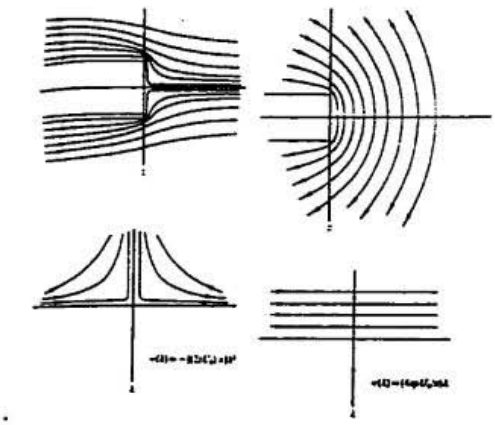

Figure 2.3: The two flows in the z and the λ-planes[30].

2.2 Derivations

2.2.1 Complex Potential

Let the complex potential due to the first flow in the transformed plane be of the form:-

$$\omega_1(\lambda) = -A_1\lambda^2 \tag{2.3}$$

From the relationship

$$u_1(z) - iv_1(z) = \frac{d\omega_1}{dz} = \frac{d\omega_1}{d\lambda}\frac{d\lambda}{dz} \tag{2.4}$$

and differentiating equation 2.3 with respect to λ. we get

$$\frac{d\omega_1(\lambda)}{d\lambda} = -2A_1\lambda \tag{2.5}$$

and equation 2.1 gives

$$\frac{d\lambda}{dz} = \frac{i\pi}{4s}\frac{1}{(1-\lambda^2)^{1/2}} \tag{2.6}$$

Therefore,

$$u_1(z) - iv_1(z) = -2A_1\lambda\frac{i\pi}{4s}\frac{1}{(1-\lambda^2)^{1/2}} \tag{2.7}$$

To find the constant A_1, we make use of the fact that at $z = \infty$ the velocity is U_0 and parallel to the x-axis. Now, as $\lambda \to \infty$, $u_1 \to U_0$, and $v_1 \to 0$. The above equation, thus, gives

$$A_1 = -\frac{2sU_0}{\pi} \tag{2.8}$$

and finally substituting the value of A_1 obtained back into equation 2.3 gives

$$\omega_1(\lambda) = (-2sU_0/\pi)\lambda^2 \tag{2.9}$$

Now, let the complex potential due to the second flow in the transformed plane be of the form:-

$$\omega_2(\lambda) = A_2\lambda \tag{2.10}$$

So the conjugate of the velocity due to ω_2 can be written as

$$u_2(z) - iv_2(z) = \frac{d\omega_2}{d\lambda}\frac{d\lambda}{dz} = A_2.\frac{i\pi}{4s}\frac{1}{(1-\lambda^2)^{1/2}} \tag{2.11}$$

At the origin, $u_2 = 0$ and $v_2 = -U_0 p$. Therefore, by substituting this condition in equation 2.11, we get A_2 as

$$A_2 = \frac{4spU_0}{\pi} \tag{2.12}$$

and so

$$\omega_2(\lambda) = (4spU_0/\pi)\lambda \tag{2.13}$$

The potential due to a point vortex of strength k_j at position λ_j is given by

$$\omega_j(\lambda) = -\frac{ik_j}{2\pi}\log(\lambda - \lambda_j) \tag{2.14}$$

To satisfy the condition of zero flow across the body, we introduce image point vortices relative to the η-axis. These image vortices in $\xi < 0$ have strengths equal in magnitude but opposite in sign to those in $\xi > 0$. The potential due to these is given by

$$\omega_j'(\lambda) = \frac{ik_j}{2\pi}\log(\lambda - \overline{\lambda_j}) \tag{2.15}$$

where $\overline{\lambda_j}$ is the conjugate of λ_j. Summing up the potentials due to the two flows and that due to point vortices, the total complex potential at a position λ in the transformed plane is given by

$$\omega(\lambda) = \omega_1(\lambda) + \omega_2(\lambda) + \sum_j \omega_j(\lambda) + \sum_j \omega_j'(\lambda) \tag{2.16}$$

i.e.,

$$\omega(\lambda) = (-2sU_0/\pi)\lambda^2 + (4spU_0/\pi)\lambda - \sum_j \frac{ik_j}{2\pi}\log\frac{(\lambda - \lambda_j)}{(\lambda - \overline{\lambda_j})} \quad \lambda \neq \lambda_j,\ \lambda \neq \overline{\lambda_j} \tag{2.17}$$

2.2.2 Vortex Velocities

Since the complex potential, $w = \phi + i\psi$, where ϕ is the velocity potential and ψ is the stream function, is a conformal invariant and the flow field due to a vortex transforms into that due to a vortex of equal strength at the transform of the vortex position, the velocity at any point in the physical plane can be obtained by transforming the positions of all the vortices into the λ -plane, determining the velocity at the transform of the required point and then returning this velocity to the physical plane using the relationship

$$u(z) - iv(z) = \frac{d\omega}{dz} = \frac{d\omega(\lambda)}{d\lambda}\frac{d\lambda}{dz} \tag{2.18}$$

Differentiating equation 2.17 with respect to λ and substituting in equation 2.18, we get the conjugate of the velocity at a location z_i as

$$\left.\frac{d\omega}{dz}\right|_{z_i} = \left[\sum_{j,j\neq i} -\frac{ik_j}{2\pi}\frac{1}{\lambda_i-\lambda_j} + \sum_j \frac{ik_j}{2\pi}\frac{1}{\lambda_i-\bar{\lambda}_j} - \frac{4sU_0\lambda_i}{\pi} + \frac{4spU_0}{\pi}\right] \times \frac{i\pi}{4s(1-\lambda_i^2)^{1/2}} \tag{2.19}$$

where λ_i is the transformed position of the location z_i.

Routh's law is then applied in the case of a point that is also a vortex position. Since the complex potential is transformal invariant. we have

$$\omega_{z_1}(z) - \frac{ik}{2\pi}log(z-z_1) = \omega_{\lambda_1}(\lambda) - \frac{ik}{2\pi}log(\lambda-\lambda_1) \tag{2.20}$$

where ω_{z_1} and ω_{λ_1} are the potentials at z_1 and λ_1 due to all causes except the vortex of strength k at z_1. Therefore we can write

$$\omega_{z_1}(z) = \omega_{\lambda_1}(\lambda) - \frac{ik}{2\pi}log(\frac{\lambda-\lambda_1}{z-z_1}) \tag{2.21}$$

Expanding $\lambda = f(z)$ in a Taylor series about z_1,

$$\lambda = f(z) = f(z_1) + (z-z_1)f'(z_1) + \frac{1}{2}(z-z_1)^2 f''(z_1) + O(z-z_1)^3 \tag{2.22}$$

or

$$\lambda - \lambda_1 = (z-z_1)f'(z) + \frac{1}{2}(z-z_1)^2 f''(z_1) + O(z-z_1)^3 \tag{2.23}$$

Substituting this into equation 2.21, we get

$$\omega_{z_1}(z) = \omega_{\lambda_1}(\lambda) - \frac{ik}{2\pi}log[f'(z_1) + \frac{1}{2}(z-z_1)f''(z_1) + O(z-z_1)^2] \tag{2.24}$$

and

$$\frac{d\omega_{z_1}}{dz} = \frac{d\omega_{\lambda_1}}{d\lambda}\frac{d\lambda}{dz} - \frac{ik}{2\pi}\left[\frac{\frac{1}{2}f''(z_1) + O(z-z_1)}{f'(z_1) + O(z-z_1)}\right] \tag{2.25}$$

Then as $z \to z_1$ and $\lambda \to \lambda_1$,

$$\left.\frac{d\omega_{z_1}}{dz}\right|_{z_1} = \left.\frac{d\omega_{\lambda_1}}{d\lambda}\right|_{\lambda_1}\left.\frac{d\lambda}{dz}\right|_{z_1} - \frac{ik}{2\pi}\frac{f''(z_1)}{2f'(z_1)} \tag{2.26}$$

This gives the expression for the conjugate velocity at a vortex position z_1 in the physical plane with a modification due to Routh's correction. Using $(dw/d\lambda)$ obtained from equation 2.17, this can be written for a vortex position z_i in general as

$$\begin{aligned}\left.\frac{d\omega}{dz}\right|_{z_i} = & \left[\sum_{j\neq i} -\frac{ik_j}{2\pi}\frac{1}{\lambda_i - \lambda_j} + \sum_j \frac{ik_j}{2\pi}\frac{1}{\lambda_i - \bar{\lambda}_j} - \frac{4sU_0\lambda_i}{\pi} + \frac{4spU_0}{\pi}\right]\left.\frac{d\lambda}{dz}\right|_{z_i} \\ & -\frac{ik_i}{2\pi}\frac{f''(z_i)}{2f'(z_i)}\end{aligned} \tag{2.27}$$

From equation 2.1, we have

$$\frac{dz}{d\lambda} = -\left(\frac{4is}{\pi}\right)(1-\lambda^2)^{1/2} \tag{2.28}$$

or

$$\frac{d\lambda}{dz} = f'(z) = \frac{i\pi}{4s}\frac{1}{(1-\lambda^2)^{1/2}} \tag{2.29}$$

Therefore,

$$\frac{f''(z)}{2f'(z)} = \frac{i\pi\lambda}{8s(1-\lambda^2)^{3/2}} \tag{2.30}$$

and so

$$\begin{aligned}\left.\frac{d\omega}{dz}\right|_{z_i} = & \left[\sum_{j\neq i} -\frac{ik_j}{2\pi}\frac{1}{\lambda_i - \lambda_j} + \sum_j \frac{ik_j}{2\pi}\frac{1}{\lambda_i - \bar{\lambda}_j} - \frac{4sU_0\lambda_i}{\pi} + \frac{4spU_0}{\pi}\right] \times \\ & \frac{i\pi}{4s(1-\lambda_i^2)^{1/2}} - \frac{ik_i}{2\pi}\frac{i\pi\lambda_i}{8s(1-\lambda_i^2)^{3/2}}\end{aligned} \tag{2.31}$$

Non-dimensionalising with respect to s and U_0 such that

$$k'_j = \frac{k_j}{U_0 s} : z' = \frac{z}{s} : u' = \frac{u}{U_0} : v' = \frac{v}{U_0} : \omega' = \frac{\omega}{sU_0}$$

we get

$$\left.\frac{d\omega'}{dz'}\right|_{z_i} = u'_i - iv'_i = -\frac{1}{(1-\lambda_i^2)^{1/2}}\left[i\lambda_i - ip - \frac{k'_i\lambda_i}{16(1-\lambda_i^2)} + \sum_j \frac{k'_j}{8}\frac{1}{\lambda_i - \overline{\lambda}_j} - \sum_{j\neq i}\frac{k'_j}{8}\frac{1}{\lambda_i - \lambda_j}\right] \tag{2.32}$$

2.2.3 Vortex Strengths

As can be seen from equation 2.32, $z = \pm is$, i.e. $\lambda = \mp 1$, are singularities of the transformation which cause infinite velocity at these points. Therefore, in-order to calculate the velocity of a newly created vortex, the velocity is calculated at the point $z' = \pm(1+\epsilon)i$ and has a strength k' equal to $\sum \frac{1}{2}U_s'^2\delta t$, where U'_s is the velocity at the point $z' = \pm(1+\epsilon)i$, δt is the time step and the summation is carried over all the time steps since the last vortex was introduced. The parameter, ϵ, is a very small number used to approximate the boundary layer thickness. However the vortices are still introduced at $z' = \pm i$, the actual separation points. This is because if the flow were a real viscous one, the velocity at the separation points would be zero to satisfy the no-slip condition and the velocity with which the newly created vortex leaves the separation point would be the velocity U'_s at the outer edge of the boundary layer. The vortex strengths can be easily derived with the help of figure 2.4.

The rate of change of circulation at point B is given by

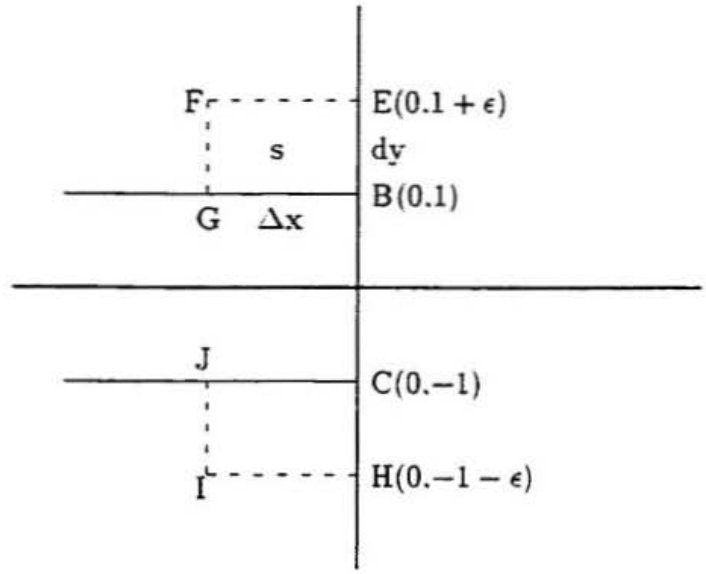

Figure 2.4: Derivation of vortex strength

$$\frac{d\Gamma}{dt} = \lim_{\Delta x \to 0} \frac{d}{dt}(\oint_C \vec{u}.d\vec{x}) \tag{2.33}$$

where C is the contour $BEFG$. Applying Green's theorem and taking $\partial v/\partial x$ to be very small in the boundary layer, we get

$$\begin{aligned}
\frac{d\Gamma}{dt} &= \lim_{\Delta x \to 0} \frac{d}{dt} \iint_s (\frac{\partial v}{\partial x} - \frac{\partial u}{\partial y}) dx dy && (2.34)\\
&\approx \int_1^{1+\epsilon} (\frac{\partial v}{\partial x} - \frac{\partial u}{\partial y}) u dy && (2.35)\\
&\approx -\int_1^{1+\epsilon} u du && (2.36)\\
&\approx -\frac{1}{2} U^2_{(1+\epsilon)} && (2.37)
\end{aligned}$$

If the vortices are shed at intervals of δt, then the strength of a nascent vortex that comes off point B is

$$k_B = \frac{d\Gamma}{dt}\delta t = -\frac{1}{2}U^2_{(1+\epsilon)}\delta t \tag{2.38}$$

Similarly, the strength of a vortex coming off point C is given by

$$k_C = \frac{d\Gamma}{dt}\delta t = \frac{1}{2}U^2_{(-1-\epsilon)}\delta t \tag{2.39}$$

2.2.4 Vortex Positions

The entire simulation is carried out in the transformed plane. The non-dimensional velocities in this plane are found using the following chain-rule

$$\frac{d\lambda'}{dt'} = \frac{d\lambda'}{dz'}\frac{dz'}{dt'} = \frac{d\lambda'}{dz'}(u'_i + iv'_i) = \frac{d\lambda'}{dz'}\left(\frac{d\omega'}{dz'}\right) \tag{2.40}$$

Once the velocities are found at all the vortex positions, the vortices are moved according to the relationships

$$\eta'(t+\delta t) = \eta'(t) + Re\left(\frac{d\lambda'}{dt'}\right)(t)\delta t \tag{2.41}$$

$$\xi'(t+\delta t) = \xi'(t) + Im\left(\frac{d\lambda'}{dt'}\right)(t)\delta t \tag{2.42}$$

During the time development of the system, some vortices were found to approach too close to the rear face of the body and this caused them to have very high velocities along the body as a result of the closeness to the single image vortices in the lower half λ-plane. To avoid this, absorption of the vortices that approached closer than $0.05s$ to the rear face was carried out by removing those vortices from the calculations. Other features of the model that were used by Clements [?] were not found to be necessary to be incorporated due to the much faster computers

available today. These features include clustering of the vortices into an equivalent single vortex of strength equal to the sum of the individual vortex strengths and position as the position of the center of vorticity of the cluster and also the shedding of the vortices at integral multiples of time steps instead of shedding vortices at every time step. A time step of $\delta t = 0.2$ was used for all calculations.

2.3 Sample Calculations

A computer program(in the C programming language) was written to simulate vortex shedding from the bluff body described earlier. Shown in figures 2.5 and 2.6 are the positions of the vortices at times $t = 5$ and $t = 10$. Also shown is the plot of the rate of change of circulation at the corners of the base of the body in figure 2.7.

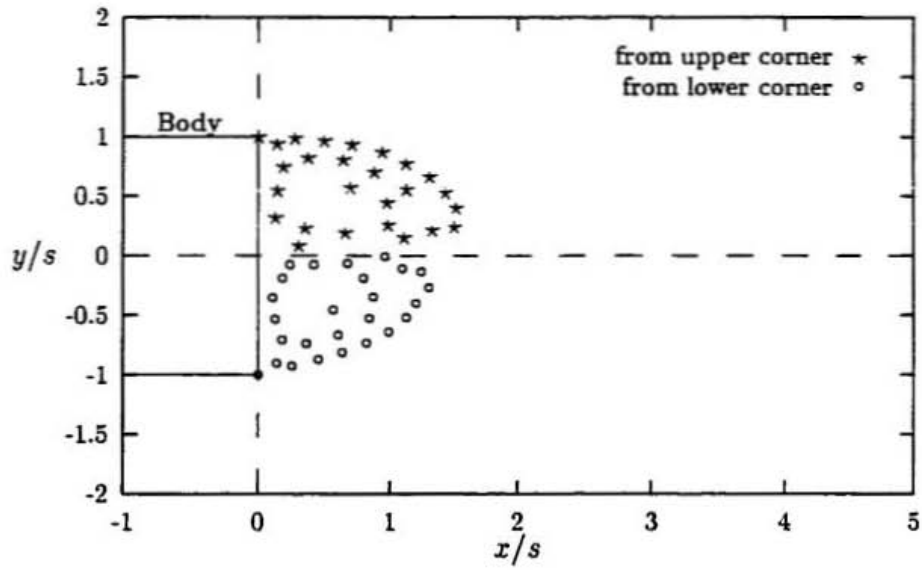

Figure 2.5: Position of the vortices at $t = 5$.

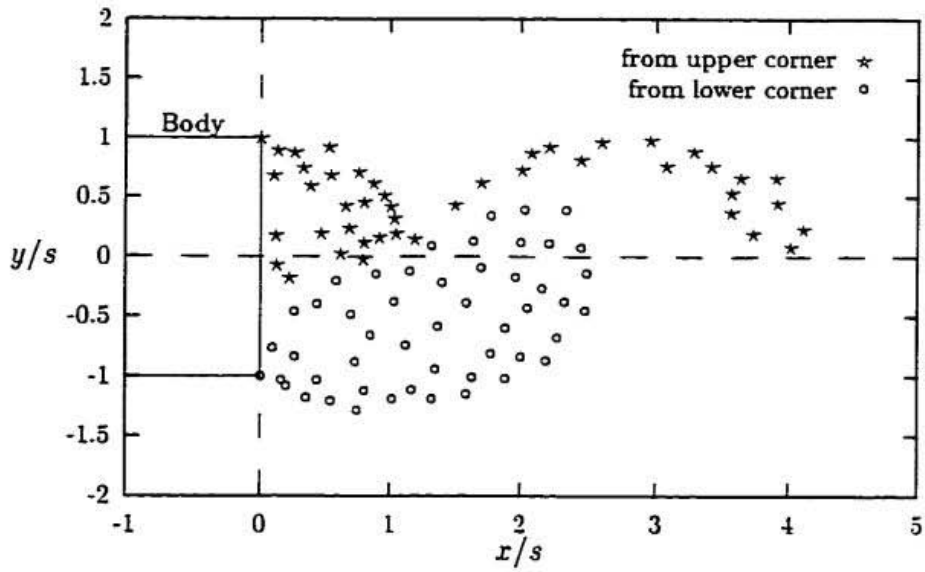

Figure 2.6: Position of the vortices at $t = 10$.

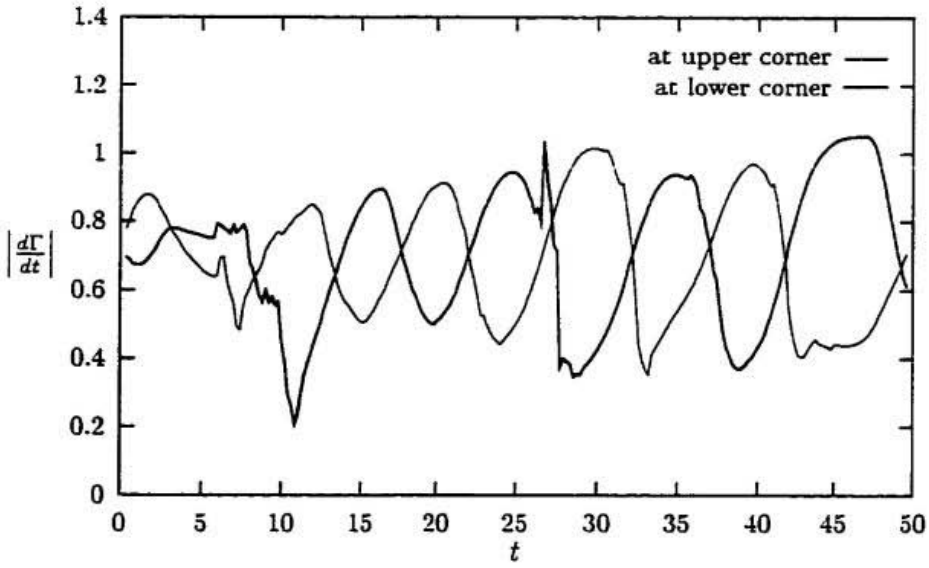

Figure 2.7: Rate of change of circulation at the corners.

Chapter 3

The Vortex-In-Cell Method

3.1 Introduction

The method described in this chapter is the Vortex-In-Cell(VIC) method developed by Christiansen [27]. This method has, since its introduction by Christiansen, been continuously improved to make it more accurate and economical with respect to computer time. In fact, this method itself is an improved version of the Random Vortex Method(RVM) of Chorin [22]. One of the advantages that the VIC method has over the RVM method is that the velocity field close to the body is better represented. This is because a mesh, that is coincident with the surface of the body, is used which enables the surface boundary conditions to be satisfied more precisely. The other advantage is that the computation time is reduced to $O(MlogM + N)$ from N^2 per time step, where M is the number of grid points and N is the number of computational elements. Also, to simulate the flow more accurately, a large number of point vortices is required. This can be efficiently handled by the vortex-in-cell method. To further reduce the computational time, an absorption procedure is used. In this procedure, the vortices that cross the body contour due to the random

walk are removed from the calculations. New particles, fewer in number than those entering the body, are introduced into the flow. They have the circulation required to compensate for that lost due to the removal of the vortices that enter the surface. This vortex method is stable, easy to set up, and accurate in predicting the detailed and highly transient flow structures which occur in the flow around a bluff body.

3.2 Theory

In this chapter, the theory for simulating flows around the section of a circular cylinder is explained. It can be further applied to other cross-section shapes, like that of a flat plate, a cylinder with a fin, and a boat-section with a skeg using conformal transformations. This is explained in the next chapter.

The Navier-Stokes equations and the continuity equation govern the flow of a viscous, incompressible and Newtonian fluid past a circular cylinder. These equations in non-dimensional form, are:-

$$\frac{\partial \vec{u}}{\partial t} = -\frac{1}{2}\nabla P - (\vec{u}.\nabla)\vec{u} + 2Re^{-1}\nabla^2\vec{u} \tag{3.1}$$

and

$$\nabla.\vec{u} = 0 \tag{3.2}$$

where $\vec{u}$ is the flow velocity, P is the pressure, Re is the Reynolds number, and t is time. These quantities are obtained by non-dimensionalising with respect to the cylinder radius (a), the uniform flow speed (U), and the density of the fluid (ρ).

$$\vec{u} = \frac{\vec{u^*}}{U}; \qquad t = \frac{t^*U}{a}; \qquad P = \frac{P^*}{\frac{1}{2}\rho U^2}$$

where u^*, P^*, and t^* are the dimensional velocity, pressure, and time respectively. However, to numerically simulate the flow, the Navier-Stokes equations can be written in the form of the Poisson equation for the stream function, ψ,

$$\nabla^2 \psi = -\omega \tag{3.3}$$

and the transport equation for the component of vorticity normal to the two-dimensional plane of flow, ω,

$$\frac{\partial \omega}{\partial t} = -(\vec{u}.\nabla)\omega + 2Re^{-1}\nabla^2\omega \tag{3.4}$$

The vorticity is given by

$$\vec{\omega} = |\nabla \times \vec{u}|\,\hat{k} \tag{3.5}$$

The flow is simulated in a polar coordinate system (r, θ) in which the cylinder surface is defined by $r = 1$. The boundary conditions for equation 3.3, immediately after the start of the flow $(t > 0)$, are

$$\psi = 0 \qquad \text{for } r \leq 1 \tag{3.6}$$

$$\textit{and} \quad \frac{\partial \psi}{\partial r} \rightarrow -sin\theta \qquad \text{as } r \rightarrow \infty \tag{3.7}$$

The boundary conditions for equation 3.4 are

$$\vec{u}.\hat{\theta} = 0 \qquad \text{for } r \leq 1 \tag{3.8}$$

$$\textit{and} \quad \omega \rightarrow 0 \qquad \text{as } r \rightarrow \infty \tag{3.9}$$

The boundary conditions given by equations 3.6 and 3.8 ensure the velocity within the cylinder surface is zero and the conditions given by equations 3.7 and 3.9 imply that the vorticity and the perturbation that it causes in the flow, at large distances from the cylinder surface, are small. The velocity $\vec{u}$ can be computed from the finite difference form of the equation

$$\vec{u} = \frac{\hat{r}}{r}\frac{\partial \psi}{\partial \theta} - \hat{\theta}\frac{\partial \psi}{\partial r} \tag{3.10}$$

where $\hat{r}$ and $\hat{\theta}$ are the unit vectors in the radial and the azimuthal directions, respectively.

3.3 The Method

The vorticity distribution in the flow, given by,

$$\omega(x, y) = \sum_{i=1}^{N} \Gamma_i \delta(x - x_i)\delta(y - y_i) \tag{3.11}$$

is represented by N point vortices. Here Γ_i is the circulation of the i^{th} vortex, (x_i, y_i) its position, and δ is the Dirac delta function. The computational domain is defined by a $m \times n$(m is typically 100 or 200 and n is 129) exponential mesh defined over an annular region, $1 < r < r_0$, together with a modified polar coordinate system (r', θ)(see below) in which the mesh size is uniform. In this system, the Poisson equation for the stream function, equation 3.3, can be written as

$$\frac{\partial^2 \psi}{\partial \theta^2} + a(r')\frac{\partial^2 \psi}{\partial r'^2} + b(r')\frac{\partial \psi}{\partial r'} = -\omega r^2 \tag{3.12}$$

where

$$\begin{aligned} a(r') &= \left(r\frac{dr'}{dr}\right)^2 \\ b(r') &= \left(r\frac{dr'}{dr}\right) + r^2\frac{d^2r'}{dr^2} \\ \text{and} \qquad r &= B(e^{Ar'} - 1) + 1 \end{aligned} \tag{3.13}$$

This equation is solved using the finite difference method and a Fast Fourier transform for the azimuthal θ-direction. A FORTRAN 77 package called FISHPACK(Version 3.1, October 1980), developed by John Adams, Paul Swarztrauber and Roland Sweet, The National Center for Atmospheric Research, Boulder Colorado, U.S.A, was used. Both $-\omega r^2$ and ψ are expanded as Fourier series in θ and substituted into the finite difference analogue of equation 3.12. This gives a set of tridiagonal simultaneous equations for each harmonic amplitude of ψ which are solved by the Gauss elimination method. The coordinate system (r', θ) is such that

$$\begin{aligned} r' &= j \qquad\qquad 0 \leq j < m \\ \theta &= i\Delta\theta \qquad\qquad 0 \leq i < n \\ \text{where} \qquad \Delta\theta &= 2\pi/(n-1) \end{aligned}$$

The coefficients A and B in equation 3.13 are found by solving the simultaneous equations obtained by taking the value of the outer radius r_0 to be r for $r' = m-1$ in equation 3.13 and the radial mesh spacing at the cylinder surface, $(r_{r'=1} - 1)$, to be equal to $\sqrt{2\nu\Delta t}$. Here, ν is the kinematic viscosity of the fluid and Δt is the time step. It is important that r_0 is chosen such that the boundary conditions, given by equations 3.7 and 3.9, hold. A value of $r_0 = 100$ was used for all the

simulations.

An area-weighting scheme, illustrated in section 1.3.3, is used to distribute the circulation carried by each vortex onto the four corner nodes of the cell in which that particular vortex is contained. Having done that, if $\Gamma(i,j)$ is the total circulation associated with the node (i,j), the value of ω at that node is given by

$$\omega(i,j) = \left.\frac{\Gamma(i,j)}{r\Delta\theta}\frac{dr'}{dr}\right|_{r'=j} \tag{3.14}$$

To model the action of viscosity at a solid boundary, new vortices are created along $r = 1$ at each time step with circulation such that the boundary condition on the tangential component of velocity, equation 3.8, is satisfied. The additional circulation, $\Gamma(i,0)$, that must be introduced at every node on the surface, is given by

$$\Gamma(i,0) = \Delta\theta\omega(i,0)\left.\frac{dr}{dr'}\right|_{r'=0} - \Gamma'(i,0) \tag{3.15}$$

Now, since $\psi = 0$ along $r = 1$, the finite difference form of equation 3.12 reduces to

$$\omega(i,0) = -a(0)[\psi(i,1) - 2\psi(i,0) + \psi(i,-1)] - \frac{1}{2}b(0)[\psi(i,1) - \psi(i,-1)] \tag{3.16}$$

Setting the stream function to be zero inside and on the surface of the cylinder, we get

$$\omega(i,0) = -[a(0) + \frac{1}{2}b(0)]\psi(i,1) \tag{3.17}$$

and $\Gamma'(i,0)$ is the circulation distributed onto the mesh, along the body contour, from the old vortices. Since the vortices are generated all over the body contour,

we do not need to determine the position of the separation points. The additional circulation is shared equally among the newly created vortices, n_v in number, at each node. An impulsive start causes a large amount of circulation to be created at each of the surface nodes at the first time-step. Therefore, to reduce the circulation carried by the initial vortices, a total of twenty new vortices were created at the first time step and three at every subsequent time step.

All the vortices, those that are already present in the flow together with those that have just been introduced on the body surface, are then moved using the Operator Splitting Technique(OST) of Chorin [23]. Equation 3.4 is split into a non-linear Euler convection equation

$$\left[\frac{\partial \omega}{\partial t}\right]_C = -(\vec{u}.\nabla)\omega \tag{3.18}$$

and a linear diffusion equation

$$\left[\frac{\partial \omega}{\partial t}\right]_D = 2Re^{-1}\nabla^2\omega \tag{3.19}$$

Equation 3.18 is solved by convecting the vortices. They are moved with velocities given by the finite difference form of equation 3.10 using the nodal values of the stream function of the cell containing the vortex. A second order Runge-Kutta method is applied. The position of a vortex after displacement due to convection from position $\vec{r_1}$ is given by

$$\vec{r_2} = \vec{r_1} + \frac{1}{2}(\vec{d_1} + \vec{d_2}) \tag{3.20}$$

where

$$\begin{aligned} \vec{d_1} &= \vec{u}(\vec{r_1}, t)\Delta t \\ \vec{d_2} &= \vec{u}(\vec{r_1} + \vec{d_1}, t + \Delta t)\Delta t \end{aligned}$$

A second solution of the Poisson equation is required for the calculation of $\vec{d}_2$.

For the solution of equation 3.19, the vortices are diffused by adding a random walk to the position of the vortices. If Δx_{diff} and Δy_{diff} are two random numbers selected from a normal distribution with a zero mean and a variance of $2\nu\Delta t$, then the position of a vortex after diffusion from the position (x_1, y_1) is given by

$$(x_2, y_2) = (x_1, y_1) + (\Delta x_{diff}, \Delta y_{diff}) \tag{3.21}$$

Since the effect of diffusion is simulated by adding a random walk to the position of the vortices using random numbers, variables such as pressure forces, vorticity, stream function, and velocity etc. all have a small random component associated with them. This random component grows with $\sqrt{\Delta t/Re}$. In other words, it decreases as the Reynolds number increases since the random walk becomes smaller.

During the process of convection, some of the vortices may enter the cylinder surface. These vortices are reflected back into the flow about the cylinder surface. Furthermore, as we deal with oscillatory flows, many vortices tend to remain close to the body contour due to the reversal of the flow. Therefore, there may be some vortices that enter the body due to the diffusion process, i.e., the random walk. These vortices, which enter the body, are coalesced at the nearest nodes of the contour mesh. New vortices are then re-injected into the fluid at a radial distance, chosen from the same distribution of random numbers as for the diffusion process, from the cylinder surface. This leads to a considerable reduction in the number of vortices present in the flow, enabling longer flow simulations in time.

3.4 Pressures, Force Coefficients and Vorticity

3.4.1 Pressures

It is known that the velocity and acceleration are equal to zero at $r = 1$. Therefore, equation 3.1 can be simplified and written as

$$-\frac{1}{2}\nabla P + 2Re^{-1}\nabla^2\vec{u} = 0 \tag{3.22}$$

or

$$\frac{1}{2}\nabla P = 2Re^{-1}\nabla^2 u = 2Re^{-1}[\nabla(\nabla.\vec{u}) - \nabla \times \nabla \times \vec{u}] \tag{3.23}$$

From the continuity equation, we have $\nabla.\vec{u} = 0$. We also have $\vec{\omega} = |\nabla \times \vec{u}|\,\hat{k}$. Substituting these in equation 3.23, we get

$$\frac{1}{2}\nabla P = 2Re^{-1}[-\nabla \times \vec{\omega}] \tag{3.24}$$

Taking a scalar product of each side of the above equation with $\hat{\theta}$ gives

$$\frac{1}{2}\frac{\partial P}{\partial \theta} = -2Re^{-1}\frac{\partial \omega}{\partial r} \tag{3.25}$$

The right hand side of equation 3.25 represents the flux of circulation per unit length across the cylinder surface, modelled over one time increment by the creation of circulation $\Gamma(i,0)$ at the surface nodes. This is given by equation 3.15. Hence, at any instant of time, the pressure distribution around the surface of the cylinder can be obtained by integrating the pressure increments along the minor arcs, $(i - 1/2)\Delta\theta < \theta < (i + 1/2)\Delta\theta$, which are given by

$$\Delta P_i = 2\Gamma(i,0)/\Delta t \tag{3.26}$$

3.4.2 Force Coefficients

The drag and lift forces are represented by their respective force coefficients, C_D and C_L. These are calculated by integrating the pressure distribution obtained from equation 3.26. They are given by

$$C_D = \frac{\Delta\theta}{\Delta t}\sum_{j=0}^{128}\left[cos(j\Delta\theta)\sum_{i=1}^{j}\Gamma(i,0)\right] \tag{3.27}$$

and

$$C_L = -\frac{\Delta\theta}{\Delta t}\sum_{j=0}^{128}\left[sin(j\Delta\theta)\sum_{i=1}^{j}\Gamma(i,0)\right] \tag{3.28}$$

Alternatively, the force coefficients can be found from the general formula for the force acting on rigid bodies in incompressible flow given by Quartepelle & Napolitano [30]. This requires the knowledge of the entire vorticity field. For our case of a cylinder in flow at a Reynolds number above 1000, the formula simplifies to the following integral expression for the drag force F_D,

$$F_D = \int_A dA(\vec{u}\times\vec{\omega}).\nabla\eta_x \tag{3.29}$$

where A is the area and

$$\eta_x = x/r^2 \tag{3.30}$$

Using equation 3.11 to discretize the vorticity field, equation 3.29 gives the following expressions for the drag and the lift coefficients

$$C_D = \sum_{i=1}^{L}\Gamma_i\left[\frac{u_i sin(2\theta_i) - v_i cos(2\theta_i)}{r_i^2}\right] \tag{3.31}$$

and

$$C_L = -\sum_{i=1}^{L} \Gamma_i \left[\frac{v_i sin(2\theta_i) + u_i cos(2\theta_i)}{r_i^2} \right] \tag{3.32}$$

where r_i is the position of the ith vortex and u_i and v_i are its velocities parallel to the flow and at right angles to it, respectively. A comparison between the time histories of the drag coefficient calculated from the integration of pressures, equation 3.27 and that obtained from the formula given by Quartepelle & Napolitano, equation 3.31, is shown in figure 3.1.

3.4.3 Vorticity

Since the area-weighting scheme smoothes the vorticity distribution along the cylinder surface, the surface vorticity $\omega_0(\theta)$ cannot be taken to be the nodal values of ω along $r = 1$. Thus, the surface vorticity is found by making use of the nodal values $\omega(i, 1)$, by using a Taylor series expansion of $\omega(r)$. The formula for the surface vorticity distribution is

$$\omega_0(i\Delta\theta) \simeq \omega(i, 1) + \frac{Re\Gamma(i, 0)}{2\Delta\theta\Delta t} \frac{dr}{dr'}\bigg|_{r'=0} \tag{3.33}$$

3.5 Some Numerical Results

A computer program(in the C programming language with calls to standard FORTRAN 77 subroutines) was developed incorporating the above method. Some flow simulations were carried out. Shown below are the plots of the time history of the drag coefficient for a submerged circular cylinder in a steady flow(figure 3.1), surface vorticity distributions at $Re = 1000$(figures 3.2, 3.3, and 3.4), surface pressure distributions at $Re = 1000$ (figures 3.5, 3.6, and 3.7), and the radial velocity on

the symmetry axis behind the cylinder(figures 3.8 and 3.9).

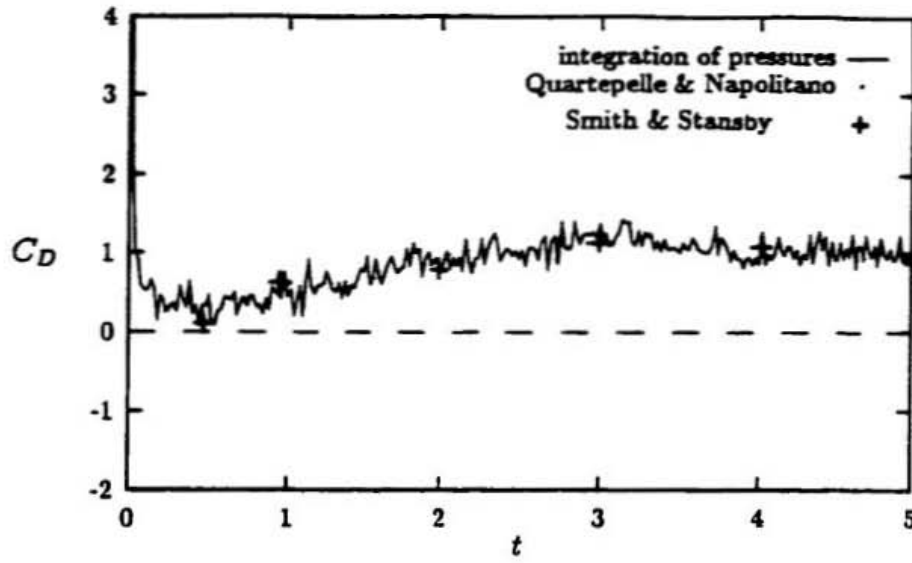

Figure 3.1: Time history of the drag coefficient at $Re = 1000$.

As can be seen from figure 3.1 , there exists a good agreement between the time histories of the drag coefficient calculated from equations 3.27(integration of pressures) and 3.31(Quartepelle & Napolitano). However, a random component is associated with the C_D calculated from equation 3.27. Shown here are also the results of Smith & Stansby [31] for comparison. More numerical experiments showed that the agreement did not significantly depend on the Reynolds number(greater than 1000). It improved by decreasing the time-step, Δt.

In figures 3.2 - 3.4 over leaf, the random component in the vorticity distribution is quite large. This can be reduced by averaging over a number of simulations or increasing n_v. The random component that is associated with the surface pressure distributions in figures 3.5 - 3.7 decreased with an increase in the Reynolds number since the random walk became smaller. It was also found that changing r_0 caused insignificant differences. So a value of $r_0 = 100$ was chosen and used for

all subsequent simulations. The curves in figures 3.8 and 3.9 were found to be

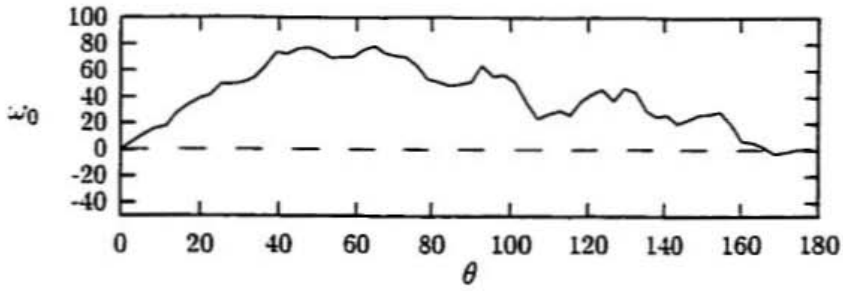

Figure 3.2: Surface vorticity distribution, $t = 0.3$.

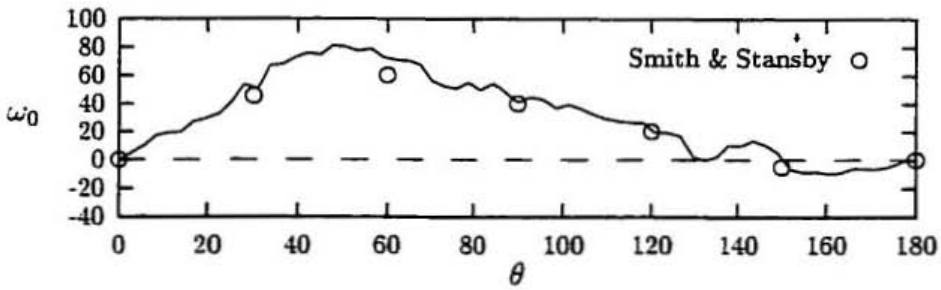

Figure 3.3: Surface vorticity distribution, $t = 0.6$.

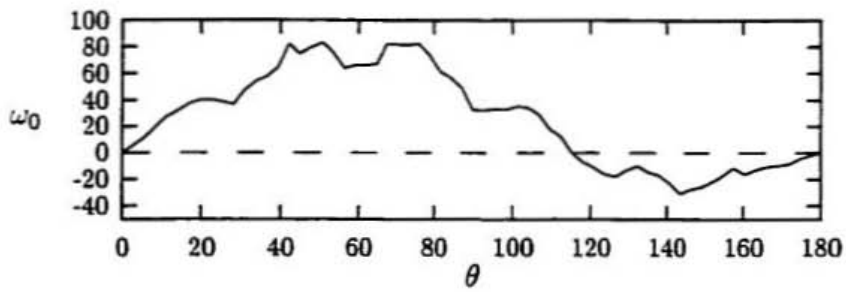

Figure 3.4: Surface vorticity distribution, $t = 0.9$.

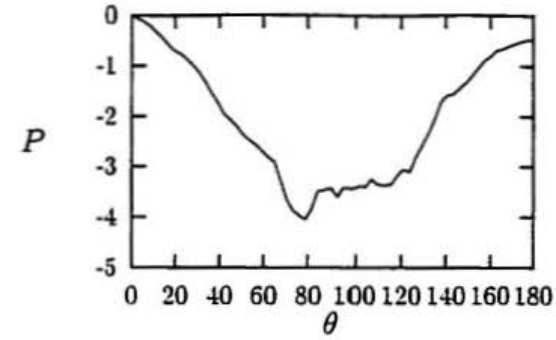

Figure 3.5: Surface pressure distribution, $t = 0.3$.

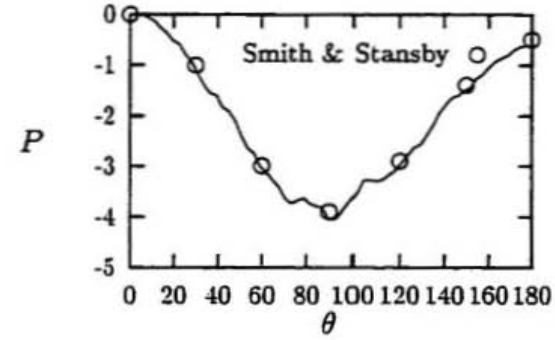

Figure 3.6: Surface pressure distribution, $t = 0.6$.

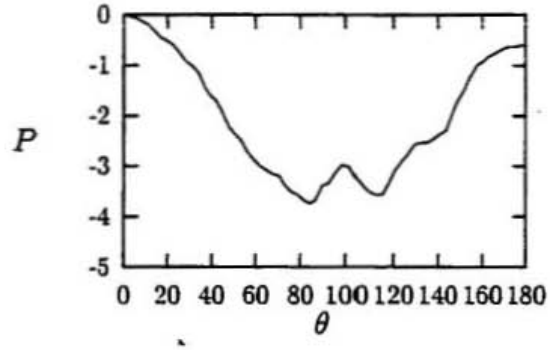

Figure 3.7: Surface pressure distribution, $t = 0.9$.

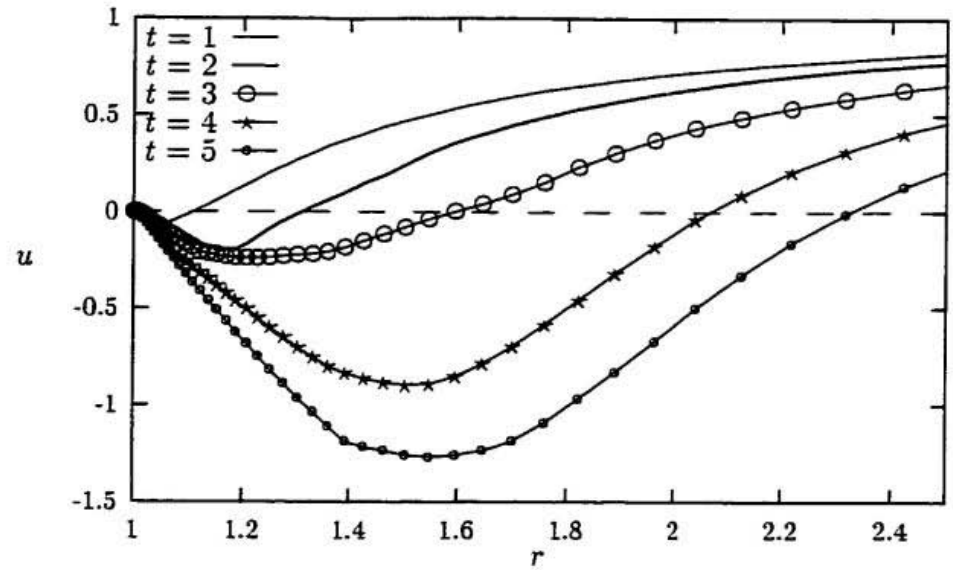

Figure 3.8: Radial velocity on the x-axis behind the cylinder, $Re = 3000$.

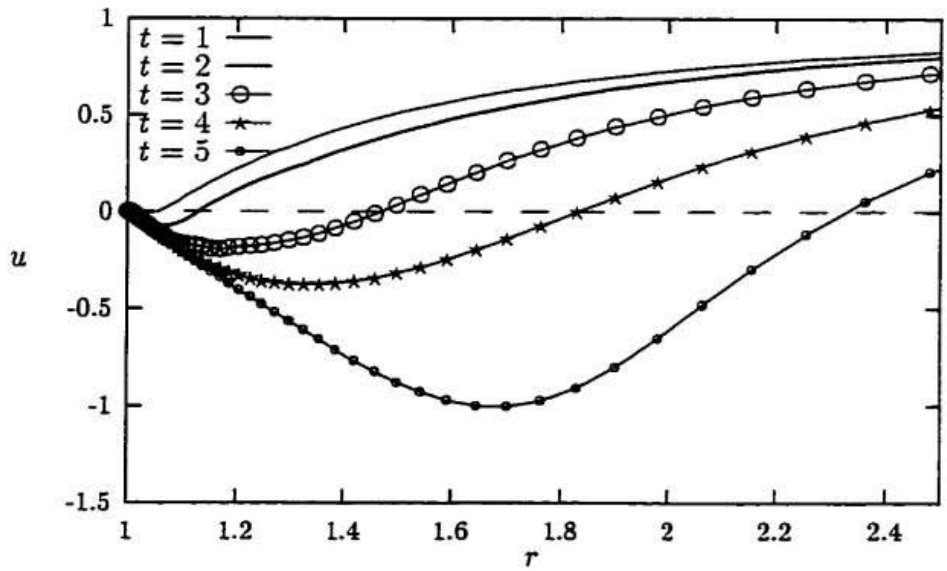

Figure 3.9: Radial velocity on the x-axis behind the cylinder, $Re = 9500$.

sensitive to the value of n_v. They improved with an increase in n_v. For the curves shown in figures 3.8 and 3.9, $n_v = 5$ was used.

The results presented in figures 3.1 - 3.9 are in very good agreement with those presented in the paper by Smith and Stansby [31], some of which are shown in figures 3.1, 3.3 and 3.6 for comparison. This provided us with a good validation of our simulation program. On the basis of this, simulations for flows past other bodies, of cross-section shapes other than that of a cylinder, were carried out with the use of conformal transformations. This is presented in the next chapter.

Chapter 4

Results using Conformal Mapping

4.1 Introduction

The method for the numerical simulation of flows past a circular cylinder was explained in the previous chapter. To study flows past bodies that have other cross-sectional shapes, the physical plane containing the body section is mapped into a plane containing a unit circle, which corresponds to the contour of the physical body. This is done by the use of conformal transformations. Generally, for the geometry of some sections that we are interested in, the transformation of the body contour onto the unit circle is a two-step procedure. First, any sharp corners, that the body may have, are removed by successive applications of the Karman-Trefftz transformation. This is referred to as the Corner Removing Procedure. The second part is to map the body, with the sharp corners removed, onto a unit circle via the Theodorsen-Garrick transformation. All the calculations are performed in the transformed plane containing the unit circle. This renders the problem as being

one of a two dimensional flow past a circular cylinder. Then, the method described in the previous chapter can be used to simulate the flow in this new plane. Any quantities calculated using the circular cylinder are then used to compute those in the physical plane using the conformal transformation and its derivative.

4.2 Modification to the VIC method

The plane containing the unit circle is referred to as the computational domain. The use of conformal transformations provides us with a concentration of mesh nodes in the neighborhood of the sharp corners in the physical plane as a result of the uniform distribution in the azimuthal, θ, direction, that is used in the computational, ζ, plane. All the formulae for the convection and diffusion of vortices, calculation of force coefficients, etc., get modified as a result of the coupling of the vortex-in-cell method with the conformal transformation. Following Scolan and Faltinsen [32], the Jacobian of the transformation is defined as the mapping derivative of the conformal transformation. It is given by

$$J = \frac{dz}{d\zeta} \tag{4.1}$$

The usual definition of the Jacobian of a transformation, however, is the ratio of an elemental area of the physical plane to that of the transformed plane, $|dz/d\zeta|^2$. The convective step becomes:

$$\Delta\zeta_C = \left|\frac{1}{J}\right|^2 W(\zeta)\Delta t \tag{4.2}$$

where $W(\zeta)$ is the complex velocity calculated in the computational domain. The modified diffusion step is given by:

$$\Delta\zeta_D = \frac{1}{J}.(\Delta x_{diff} + i\Delta y_{diff}) \tag{4.3}$$

where Δx_{diff} and Δy_{diff} are, as explained in the previous chapter, a pair of random numbers belonging to a normal distribution of random numbers with zero mean and a variance of $2\nu\Delta t$.

The non-dimensional pressure force, according to [32], is given by

$$\frac{F_p}{\frac{1}{2}\rho U^2 L} = \frac{\Delta\theta}{\Delta t}\sum_{k=0}^{128}[J(\theta)e^{i\theta}]_{\theta=k\Delta\theta}\sum_{i=0}^{k}\Gamma_i \tag{4.4}$$

where ρ is the density of the fluid, U is the magnitude of the flow velocity at infinity, L is the characteristic body length, and Γ_i is the newly created circulation at the ith node on the body contour. Similarly, the non-dimensional skin friction force, according to [32], is given by

$$\frac{F_f}{\frac{1}{2}\rho U^2 L} = \frac{2i\Delta\theta}{Re}\sum_{k=0}^{128}\left[\frac{\omega_0 e^{i\theta}}{J^*(\theta)}\right]_{\theta=k\Delta\theta} \tag{4.5}$$

where ω_0 denotes the vorticity calculated at the kth node on the body surface and $J^*(\theta)$ is the complex conjugate of $J(\theta)$.

It can be seen that the convection and the diffusion displacements are significantly affected by the singular behavior of J, i.e., as $|J| \to 0$. Also affected is the normal pressure force which tends to zero as J vanishes. Since the Jacobian of the transformation vanishes at sharp corners of the body, a modification of the Jacobian is found to be necessary there. This is basically a truncation of the real part of the Jacobian in the vicinity of a sharp edge or corner to a small finite value. Shown in figure 4.1 is the effect of this value of truncation(minimum J) on the drag and mass coefficient calculations for a finned-circle at a $Re = 426$ and

$KC = 1.33$. As can be seen, the force coefficients did not vary much as a result of a variation in the truncation value. On the other hand, Scolan and Faltinsen [32] have observed large variations with the value of truncation used for a flat plate.

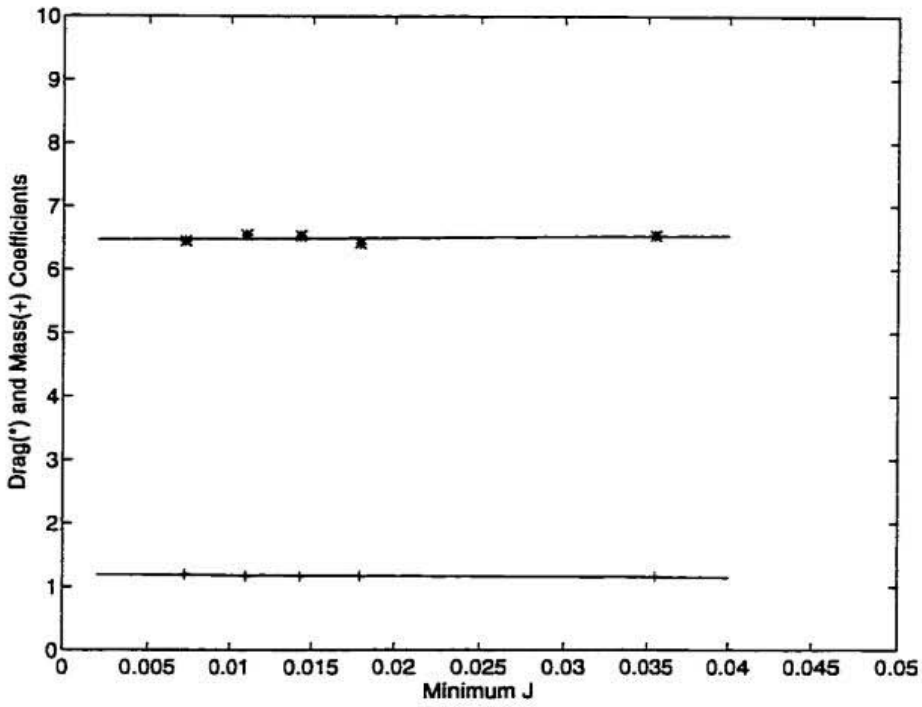

Figure 4.1: Effect of the truncation value of J on C_D and C_M

This value is determined by studying the Jacobian of the transformation for similar shapes that have rounded corners instead of sharp edges. For example, for the case of a flat plate, the similar shape used is an ellipse [32]. The shape with the sharp edges is the limiting case of the shape with the rounded corners. The value is taken to be the value of the Jacobian of the transformation, for the similar shape, at the location of the sharp corner in the actual body. Thus, to avoid the Jacobian of the actual transformation from vanishing at a sharp corner, it is assigned this finite value in a small area in the neighborhood of the corner. This treatment of the

Jacobian does not affect the direction of motion of the vortices due to convection since only its magnitude is used in the convection step as seen in equation 4.2. It can also be seen that the motion due to diffusion is not as seriously affected as the one due to convection, since only $1/J$ appears in equation 4.3, whereas $|1/J|^2$ appears in equation 4.2. Care is also taken to make the velocity at infinity the same in both the computational and the physical domains. This is ensured by forcing the value of $|J|$ at infinity($|J_\infty|$) to be unity. This, in turn, is achieved by normalizing the conformal map by the value of $|J_\infty|$. Even though the truncation keeps J from vanishing at the sharp corners, it is still a very small value. Vortices present near the sharp edges could still have displacements that are large enough to cause numerical difficulties, owing to the presence of J^{-1} in the equations 4.2 and 4.3. In order to avoid this, a maximum motion due to convection was imposed. It was fixed as $|\Delta\zeta_C|_{max}/L = 3$ for all the flow simulations. This treatment does not have a noticeable effect on the results.

Having obtained the non-dimensional forces, we can now compute the force coefficients, C_D and C_M. According to Morison's equation [32], we have

$$F(t) = \frac{1}{2}\rho C_D L u(t)\,|u(t)| + \frac{\pi}{4}\rho L^2 C_M \frac{du(t)}{dt} \tag{4.6}$$

where F(t) is the instantaneous force calculated in the direction of the flow and $u(t)$ is the flow velocity, given by

$$u(t) = U sin(\hat{\omega} t) \tag{4.7}$$

where U is the flow velocity at infinity and $\hat{\omega}$ its frequency. The force coefficients are determined by Fourier-averaging over one cycle.

$$C_D = \frac{1}{\frac{1}{2}\rho U^2 L}\frac{3\tilde{\omega}}{8}\int_0^T F(t)sin(\tilde{\omega}t)dt \tag{4.8}$$

and

$$C_M = \frac{1}{\frac{1}{2}\rho U^2 L}\frac{KC\tilde{\omega}}{\pi^3}\int_0^T F(t)cos(\tilde{\omega}t)dt \tag{4.9}$$

where T is the time period of the oscillatory flow, given by

$$T = \frac{2\pi}{\tilde{\omega}} \tag{4.10}$$

and KC is the Keulegan-Carpenter number, defined as

$$KC = \frac{UT}{L} \tag{4.11}$$

The force, $F(t)$, is taken to be the sum of the pressure and the skin friction forces in the direction of the flow.

Various cross-sections were studied by combining the VIC method with their respective conformal transformations. These are described below along with the results of some numerical examples.

4.3 Circular cylinder in oscillatory flow

This is the simplest case possible as the transformation transforms the circular cross-section onto itself. Hence $\zeta = z$ and $J = 1$ and the formulae present in the last chapter are applicable, as they are, without any modifications. Shown in figure 4.2 is the mesh generated in the plane containing the circular cylinder.

Simulations were carried out at various KC numbers at a constant value of β(the Stokes parameter, defined as $\beta = Re/KC$). Curves of C_D and C_M vs. the

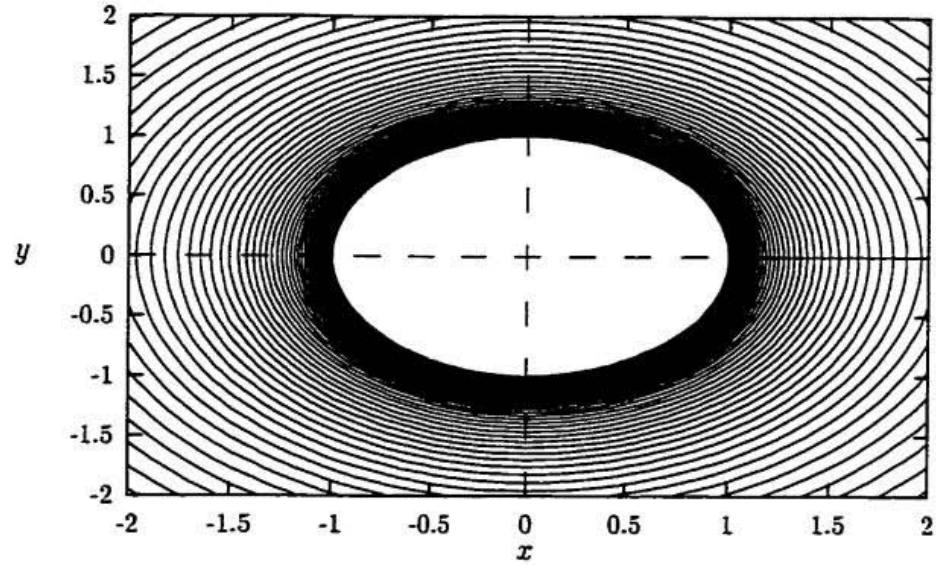

Figure 4.2: Mesh in the physical plane(circular cylinder).

KC number were plotted using the values obtained from the method together with available experimental results [34]. These are shown in figure 4.3. Also shown is the time history of the force, $F(t)$(non-dimensional), in comparison with the force as obtained from the fitting to Morison's equation(figure 4.4) for $C_D = 0.9$, $C_M = 2.0$, at $KC = 2$, $\beta = 439$, and $\hat{\omega} = 1.571$. As can be seen, the fitting was found to be very good.

4.4 Flat plate in cross oscillatory flow

As described in the introduction, all the calculations are performed in the computational dcmain that contains a unit circle which corresponds to the actual physical body. The transformation that maps the unit circle to the flat plate is given by

$$z = \frac{1}{2}(\zeta - \frac{1}{\zeta}) \tag{4.12}$$

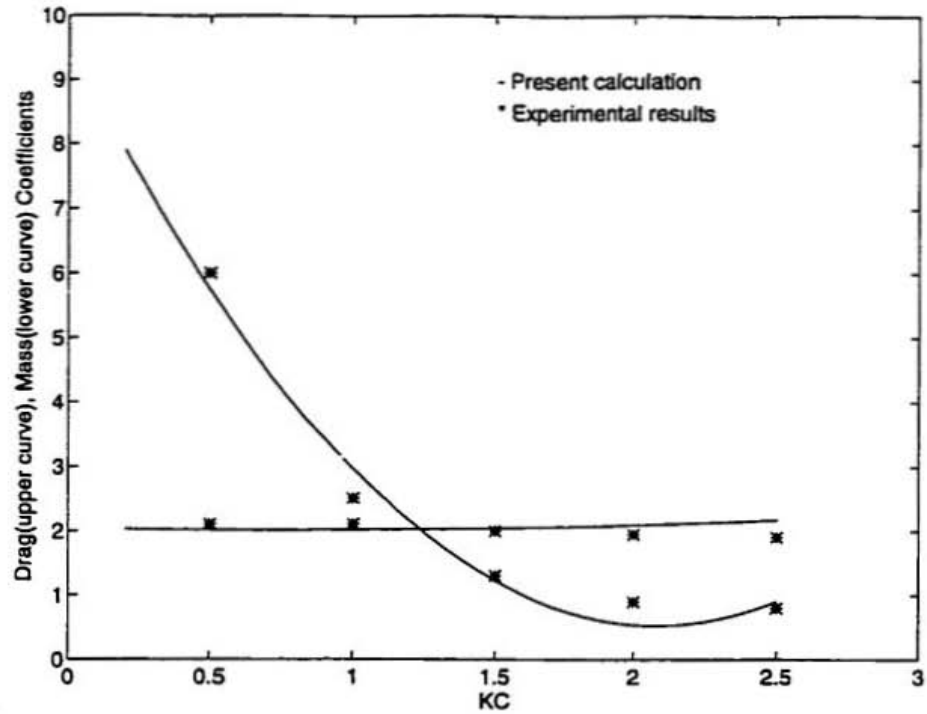

Figure 4.3: C_D, C_M *vs.* KC(circular cylinder), $\beta = 439$

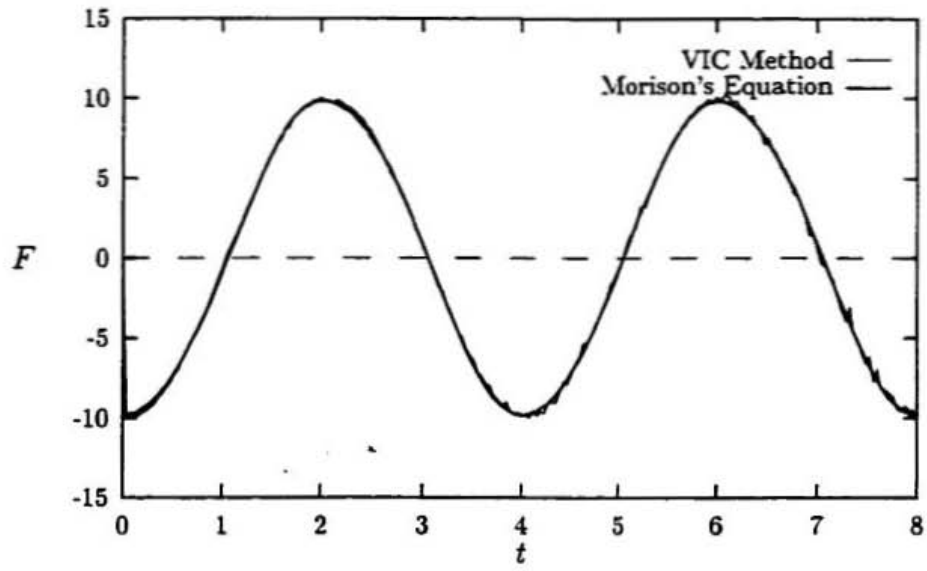

Figure 4.4: Fitting of $F(t)$ to Morison's equation(circular cylinder).

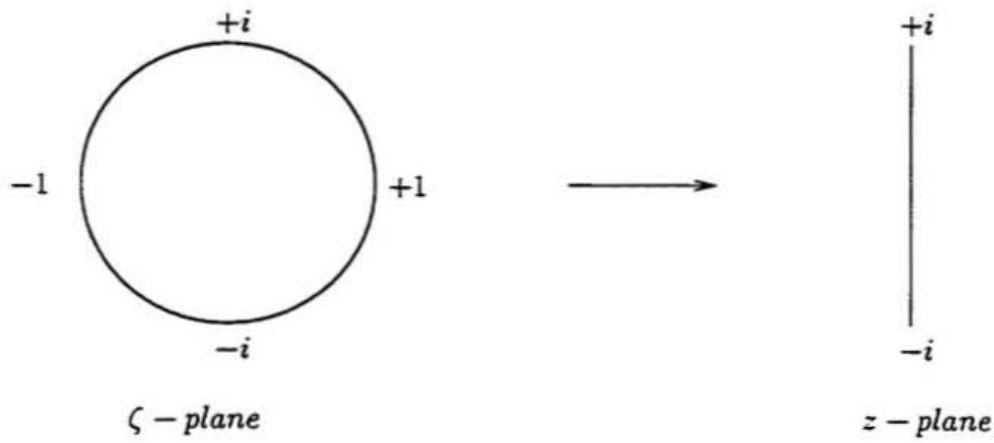

Figure 4.5: Transformation scheme for a circle to a flat plate.

$$J = \frac{dz}{d\zeta} = \frac{1}{2}(1 + \frac{1}{\zeta^2}) \tag{4.13}$$

Now as $\zeta \to \infty$,

$$|J| \to 1 = |J_\infty| \tag{4.14}$$

Here, the Jacobian vanishes at $\zeta = \pm i$. Thus, a truncation of the Jacobian, as described earlier, is necessary in the neighborhood of $\zeta = \pm i$ to avoid an infinite value of J^{-1} which is used in the convection and diffusion displacement step calculations. Figure 4.5 shows the transformation scheme of the body in the computational plane to the one in the physical plane. Figure 4.6 shows the mesh generated in the physical plane containing the flat plate.

The curves of C_D and C_M versus the KC number for the flat plate in cross flow are presented in figure 4.7 and the comparison of $F(t)$ as obtained from the method with that obtained from Morison's equation in figure 4.8 for $C_D = 15.29$, $C_M = 1.84$, at $KC = 2$, $\beta = 439$, and $\hat{\omega} = 0.785$.

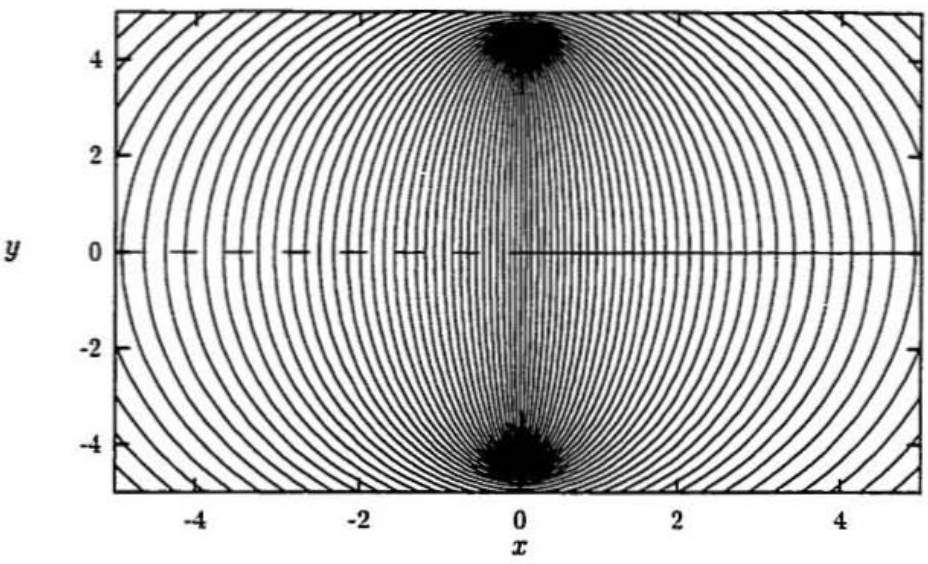

Figure 4.6: Mesh in the physical plane(flat plate).

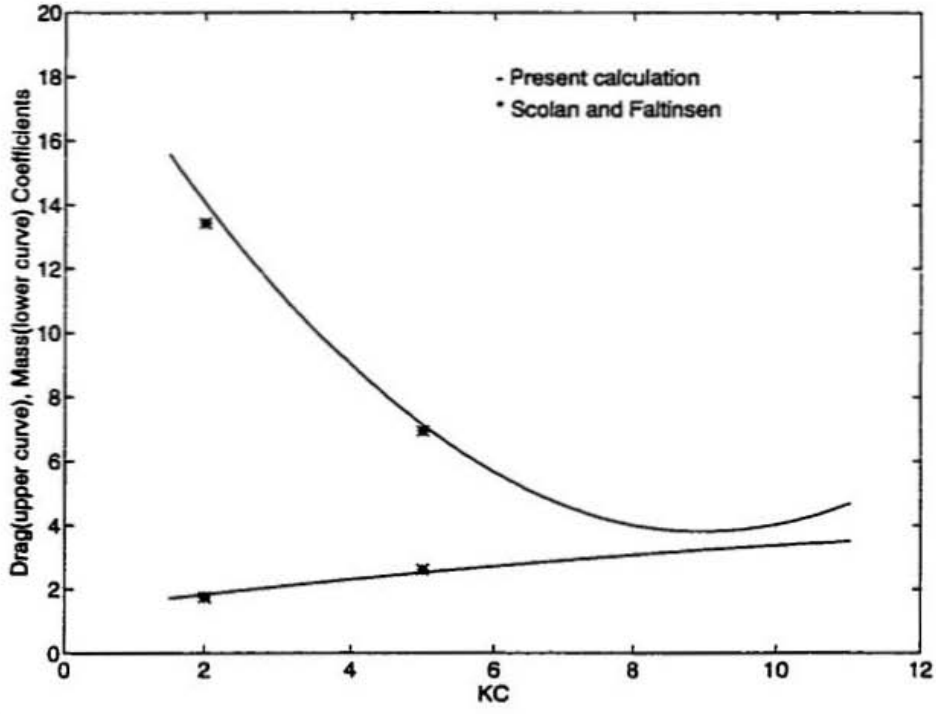

Figure 4.7: C_D, C_M *vs.* KC(flat plate), $\beta = 439$

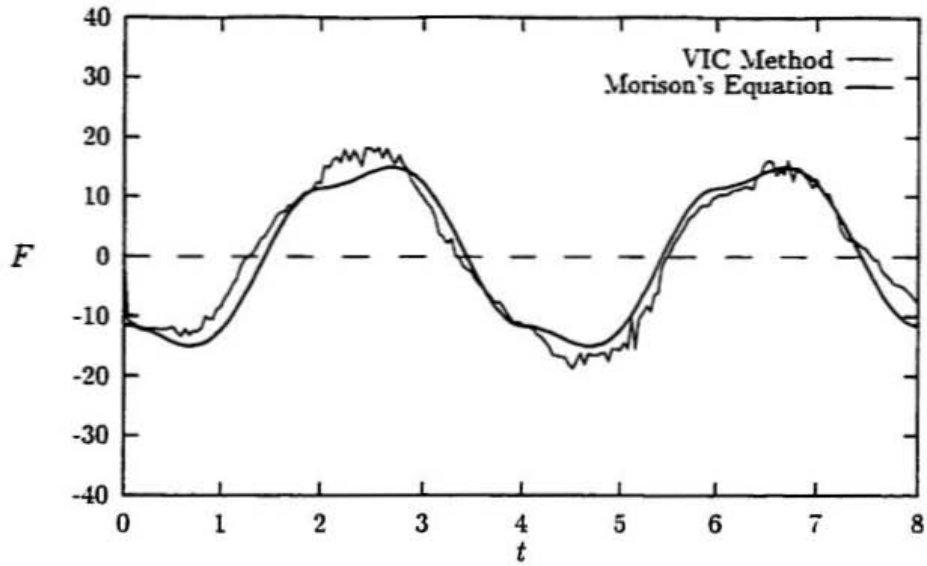

Figure 4.8: Fitting of $F(t)$ to Morison's equation(flat plate).

4.5 Cylinder with a fin

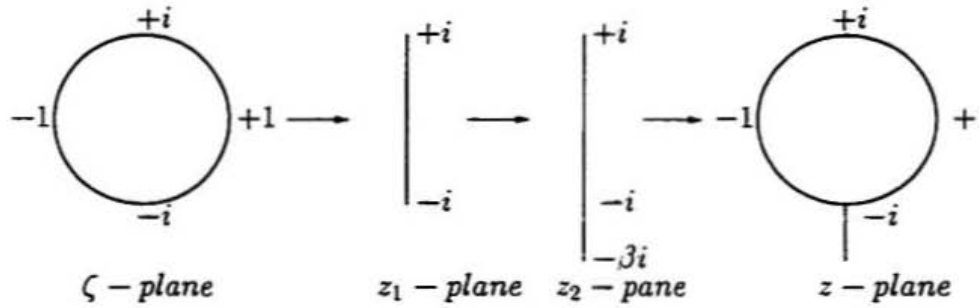

Figure 4.9: Transformation scheme for a circle to a finned-circle.

To obtain a cylinder with a fin attached to it, we first transform the circle onto a flat plate and then elongate the flat plate. This is done using the following transformations

$$z_1 = \frac{1}{2}(\zeta - 1/\zeta) \tag{4.15}$$

$$z_2 = \frac{(z_1 - i)(\beta_f + 1)}{2} + i \tag{4.16}$$

where β_f is an elongation factor. If greater than unity, the plate in the z_1-plane is elongated below the real axis in the z_2-plane. The elongated plate is then mapped onto a finned-circle with the transformation

$$z = z_2 + \sqrt{z_2^2 + 1} \tag{4.17}$$

As the objective of this study is to analyze viscous flows past floating or surface piercing bodies, we assume that the wave-making effects can be determined separately and superimposed on the viscous part solution. Since only the flow in the lower half plane is required, the free-surface is treated as a solid boundary by using symmetry about the free-surface line. This results in a flow in the upper half plane that is the image of the flow in the lower half plane past a body that is also symmetric as shown in figure 4.10.

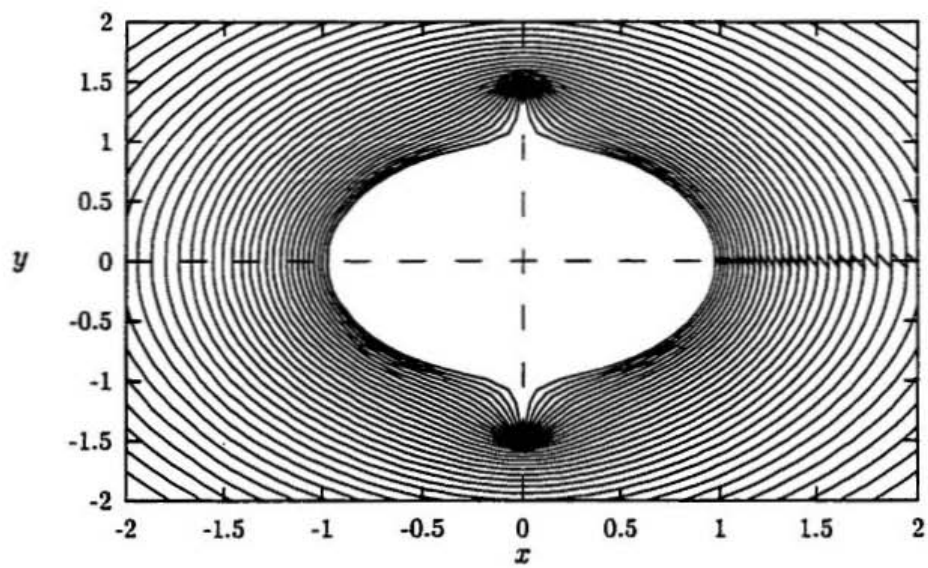

Figure 4.10: Mesh in the physical plane(finned-circle).

With these transformations at hand, we can now derive the Jacobian for the overall transformation using the chain rule

$$J = \frac{dz}{d\zeta} = \frac{dz_1}{d\zeta}.\frac{dz_2}{dz_1}.\frac{dz}{dz_2} \tag{4.18}$$

Therefore,

$$J = \frac{1}{2}(1+\frac{1}{\zeta^2})(\frac{\beta_f+1}{2})(1+\frac{z_2}{\sqrt{z_2^2+1}}) \tag{4.19}$$

$$= (\frac{\beta_f+1}{4})(\frac{\zeta^2+1}{\zeta^2})(\frac{z}{\sqrt{z_2^2+1}}) \tag{4.20}$$

and as $\zeta \to \infty$,

$$|J| \to \frac{\beta_f+1}{2} = |J_\infty| \tag{4.21}$$

The curves of C_D and C_M versus KC, obtained from the VIC method coupled with conformal transformations, are shown in figure 4.11. Figure 4.12 shows the comparison of the force $F(t)$ obtained from the method with that obtained from Morison's equation for $C_D = 6.54$, $C_M = 1.16$, at $KC = 1.33$, $\beta = 320$, and $\hat{\omega} = 1.571$. Figure 4.13 shows the streak plot in an oscillatory flow, $Re = 426$ and $KC = 1.33$, past a finned-cylinder at a non-dimensional time of 8.0(twice the period of oscillation of the flow).

4.6 Boat Sections.

By using the transformation of the circle onto a circle with a fin, it is possible to map the resulting finned-circle onto a section of a boat with a skeg. Boat sections could be rounded or have hard chines. Different transformations are used to obtain

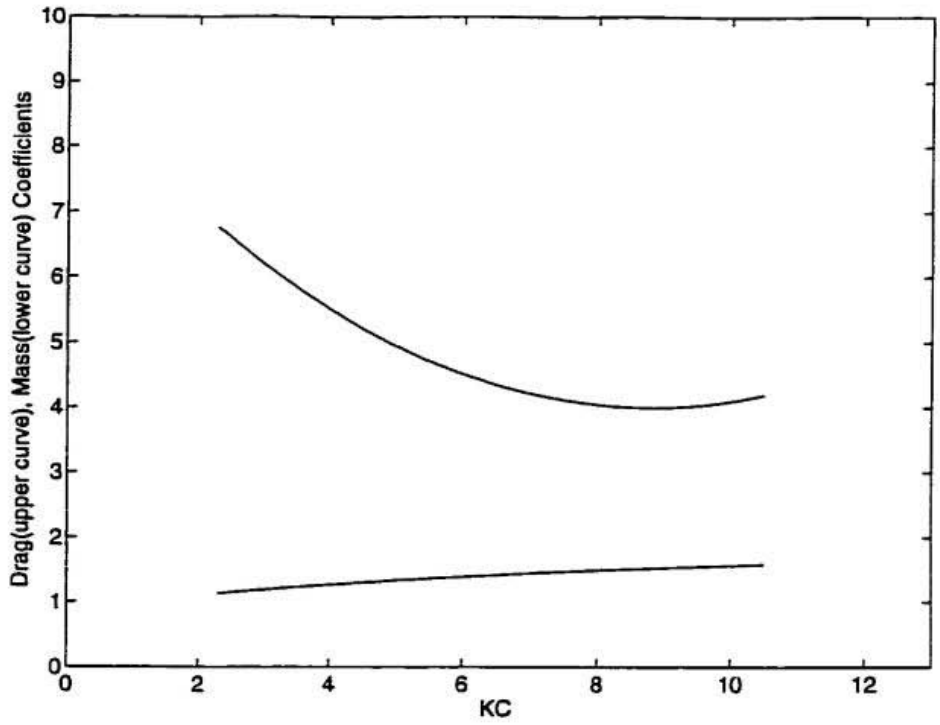

Figure 4.11: C_D, C_M *vs.* KC(finned-circle), $\beta = 320$, fin-length=0.5

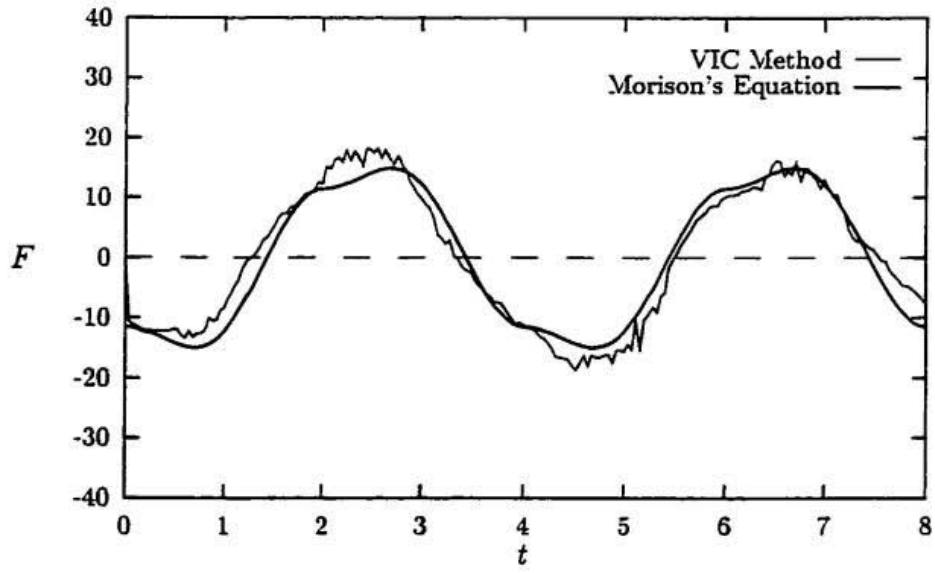

Figure 4.12: Fitting of $F(t)$ to Morison's equation(finned-circle).

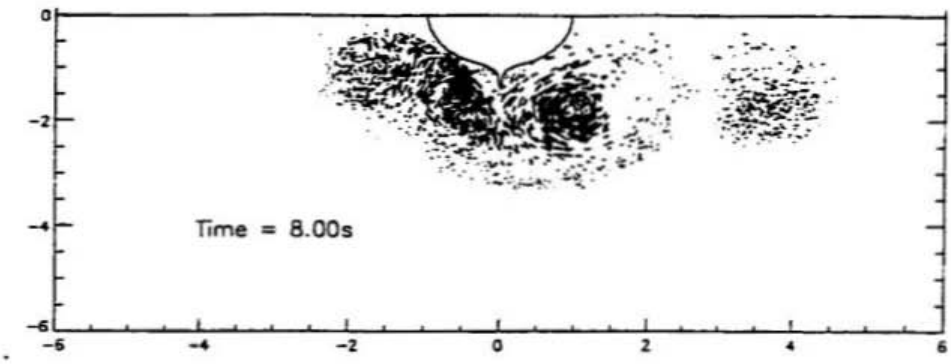

Figure 4.13: Streak plot for a finned-cylinder at $Re = 426, KC = 1.33, \Delta t = 0.04$

these two kinds of shapes. First, any sharp edges, that may be present in sections with hard chines, have to be removed. This is not required for sections that are already rounded.

4.6.1 Rounded sections

One of the standard ways of transforming a unit circle onto a boat section is through the transformation given by

$$z = \zeta + \frac{a_1}{\zeta} + \frac{a_3}{\zeta^3} \tag{4.22}$$

in which a_1 and a_3 are real and related by

$$b = 1 + a_1 + a_3 \tag{4.23}$$

$$H = 1 - a_1 + a_3 \tag{4.24}$$

where b is the half beam of the section at the required waterline and H is the draft at that waterline. Ship-sections derived using the above transformation are called Lewis forms. They have the drawback that they cannot represent ship sections

with area coefficients close to unity. Also, the Lewis transformation cannot produce the actual section shape but simply generates a section that has the same beam, draught, and sectional area. For better results, an extension of the Lewis form can be used [35]. Here the transformation has an extra parameter a_5. It is of the form

$$z = \zeta + \frac{a_1}{\zeta} + \frac{a_3}{\zeta^3} + \frac{a_5}{\zeta^5} \tag{4.25}$$

where a_1, a_3, and a_5 are real and related by the equations

$$b = 1 + a_1 + a_3 + a_5 \tag{4.26}$$

$$H = 1 - a_1 + a_3 + a_5 \tag{4.27}$$

Further, defining the parameters α, λ, σ, and η as

$$\alpha = \frac{2}{b}; \quad \lambda = \frac{H}{b}; \quad \sigma = \frac{S}{2bH}; \quad \eta = \frac{I}{bH^3} \tag{4.28}$$

where S is the sectional area of the form and I is the second moment of area of the waterplane, given by

$$I = \frac{2}{3}\int_0^b y^3 dx \tag{4.29}$$

The expression that relates α, λ, σ, and a_5 is

$$\sigma = \frac{\pi}{8\lambda}\left[-\alpha^2(1+3a_5^2) + \alpha[3(1+\lambda) + a_5(1-\lambda)] - 2(1+\lambda+\lambda^2)\right] \tag{4.30}$$

These two transformations are based on the assumption that a ship-section that has the same principal geometrical characteristics as a member of the particular family(the Lewis forms or the more general three-parameter forms) will have the

same added mass coefficients as that member. As this assumption is quite crude, a third and more accurate method of transforming a unit circle onto a ship-section is a numerically determined conformal mapping. The offsets of the section are spline-fitted so as to be able to interpolate and obtain intermediate offsets. A total of one hundred and twenty-eight offset points were generated from the given offsets. With the availability of high speed computers, it is possible to have a large number of coefficients in the transformation function. A transformation function of the form of equation 4.33 was used with a total of sixty-four, $a_0, a_1, \ldots\ldots, a_{63}$, complex coefficients. These coefficients were determined using the method of minimizing the sum of the squares of m nonlinear functions in n variables by a modification of the Levenberg-Marquardt algorithm. A FORTRAN 77 package called MINPACK, developed by Burton S. Garbow, Kenneth E. Hillstrom and Jorge J. More of the Argonne National Laboratory was run on a DEC 3000(Alpha microprocessor) computer. The non-linear functions are given by

$$f_j = x_j - Re(z_j) \qquad \text{j=1.....128} \tag{4.31}$$

$$f_{j+128} = y_j - Im(z_j) \tag{4.32}$$

where (x_j,y_j) are the coordinates of the j^{th} offset, and $Re(z_j)$ and $Im(z_j)$ are the real and imaginary components of the point generated by the transformation for a given set of values for the complex coefficients, a_i. If the section to be analyzed has a skeg, then the finned-circle, instead of the unit circle, is used to generate the boat-section. The transformation function is

$$z = a_0 \left(z_3 + \sum_{i=1}^{63} \frac{a_i}{z_3^{(2i-1)}} \right) \tag{4.33}$$

where z_3 is the plane containing the finned-circle. The mesh in the physical plane resulting from this transformation is shown in figure 4.14, for a section with no skeg.

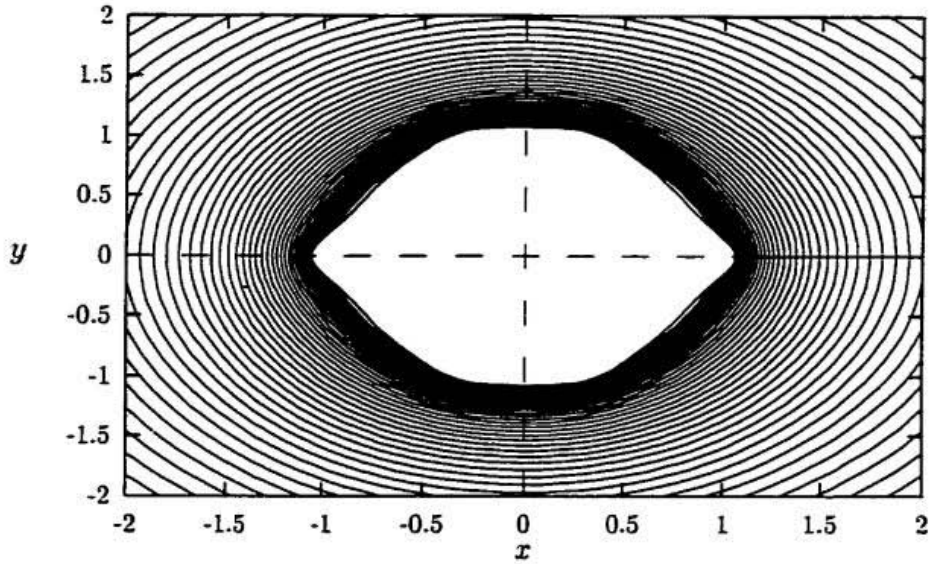

Figure 4.14: Mesh in the physical plane(rounded section, no skeg).

The Jacobian of this transformation can be written as

$$J = \frac{dz}{dz_3} = a_0 \left(1 - \sum_{i=1}^{63} \frac{(2i-1)a_i}{z_3^{2i}}\right) \tag{4.34}$$

Since the calculations are performed in the ζ-plane, the plane containing a unit circle, the overall transformation to the physical plane consists of all the intermediate transformations of the circle(ζ-plane) onto a flat plate(z_1-plane), elongation of the flat plate(z_2-plane), mapping of the elongated plate onto a circle with a fin(z_3-plane), and finally the mapping of the finned-circle onto the boat-section with a skeg(z-plane). The overall Jacobian is the product of the Jacobian obtained in the previous section(for a circle to a finned-circle) and that derived in this section. Hence the overall Jacobian can be written as

$$J_{overall} = a_0 \left(\frac{\beta_f + 1}{4}\right)\left(\frac{\zeta^2 + 1}{\zeta^2}\right)\left(\frac{z_3}{\sqrt{z_2^2 + 1}}\right)\left(1 - \sum_{i=1}^{63} \frac{(2i-1)a_i}{z_3^{2i}}\right) \tag{4.35}$$

To ensure a uniform velocity of unity at infinity in the physical plane, the Jacobian at infinity is calculated. As $\zeta \to \infty$, we have $|J_{overall}| \to a_0(\beta_f + 1)/2$. Therefore,

$$|J_\infty| = \frac{a_0(\beta_f + 1)}{2} \tag{4.36}$$

The conformal map used in the calculation procedure is normalized with respect to $|J_\infty|$. This obviates the need to modify U in the Reynolds number used in the computational domain. This would otherwise be necessary because of the change in the span of the body from the physical plane to the computational domain due to the transformation.

Flow simulations were carried out at different KC numbers, first for a boat section without a skeg by taking $\beta_f = 1$. Figure 4.15 shows the curves of C_D and C_M versus KC that were obtained using the above transformations. Figure 4.16 shows a comparison of the forces obtained from the simulation with that obtained from Morison's equation for a C_D value of 1.66 and $C_M = 1.76$, at $KC = 1.6$, $\beta = 400$, and $\hat{\omega} = 1.571$.

A fin was added to the body, to simulate the effect of a skeg, by taking the value β_f to be 1.0833. The mesh in the physical plane is shown in figure 4.17. The section gets distorted from being a flat bottom one to the one as shown due to the fairing required by the addition of the skeg. Figures 4.18 and 4.19 show the curves of C_D and C_M against KC and the comparison of forces computed from the method with that computed from Morison's equation at $C_D = 9.42$, $C_M = 1.09$, $KC = 1$, $\beta = 878$, and $\hat{\omega} = 2.094$, respectively.

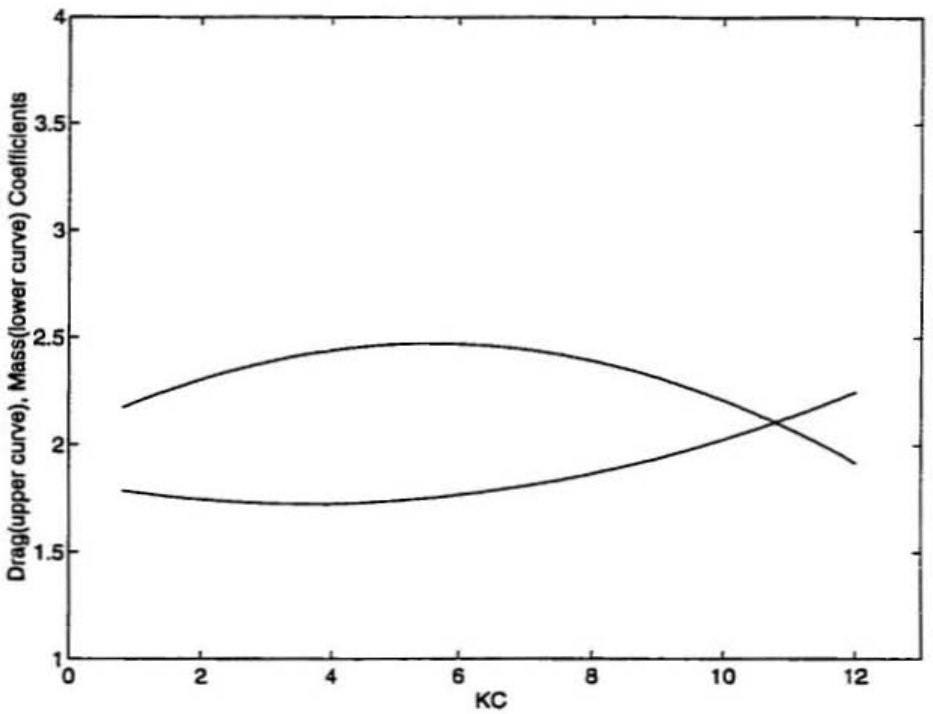

Figure 4.15: C_D, C_M *vs.* KC(rounded section, no skeg), $\beta = 400$

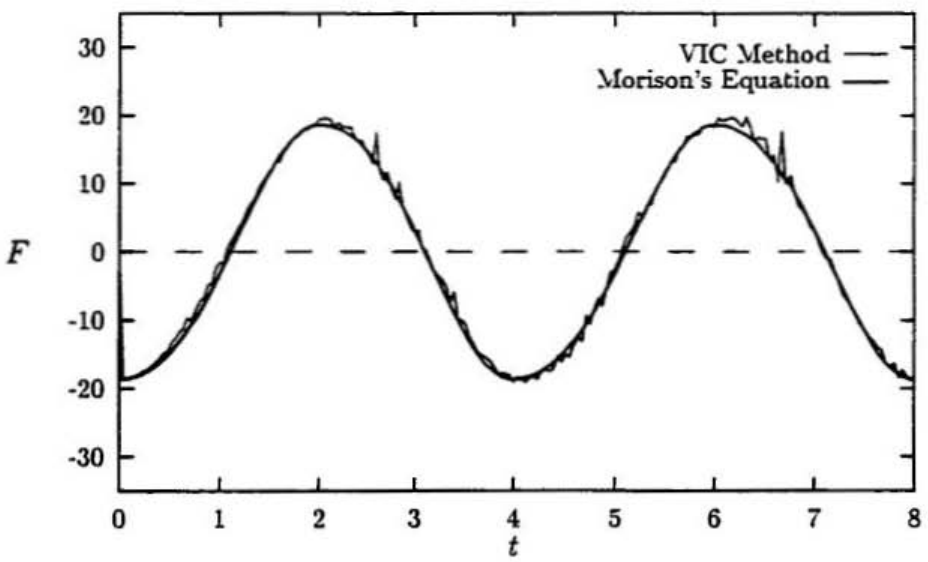

Figure 4.16: Fitting of $F(t)$ to Morison's equation(rounded section, no skeg).

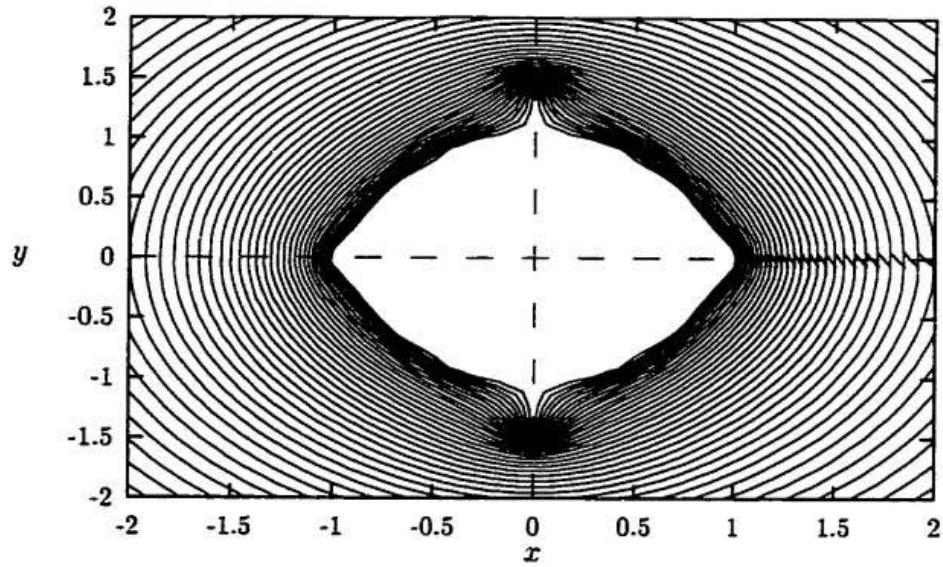

Figure 4.17: Mesh in the physical plane(rounded section, with skeg).

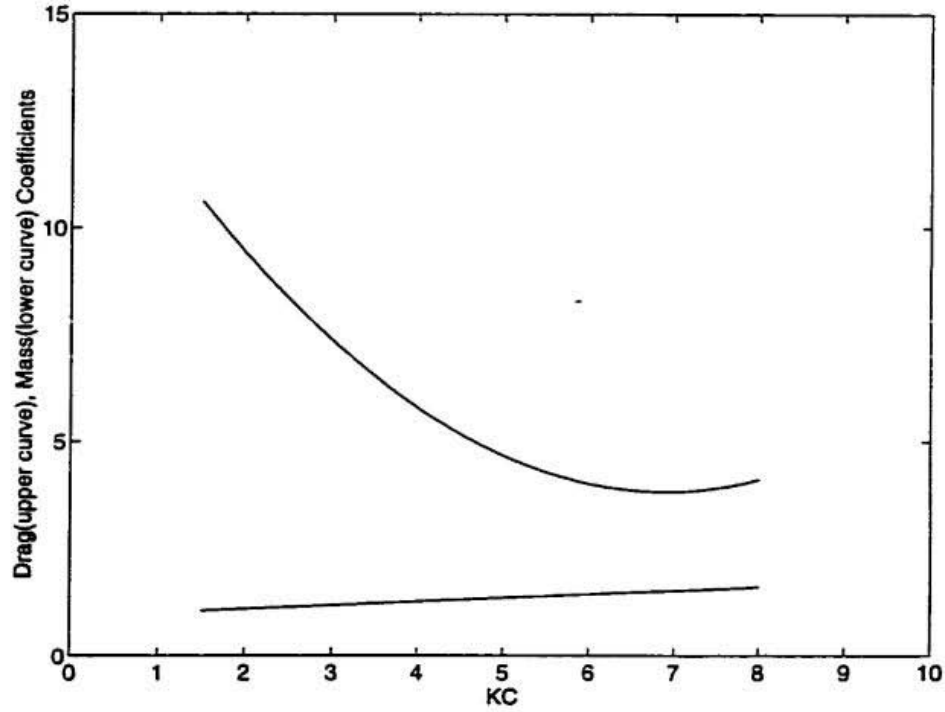

Figure 4.18: C_D, C_M *vs.* KC (rounded section, with skeg), $\beta = 878$, fin-length=0.5

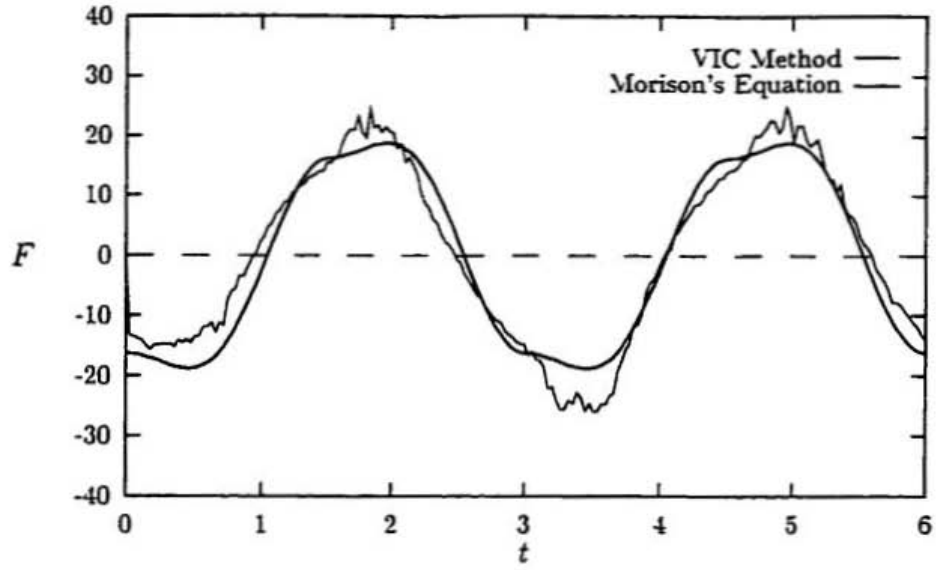

Figure 4.19: Fitting of $F(t)$ to Morison's equation(rounded section, with skeg).

4.6.2 Sections with sharp edges(hard chines)

As these sections have sharp edges, we follow the two step procedure mentioned in the introductory section of this chapter. This is based on the method that was introduced by Ives [33]. The method is illustrated below in figure 4.20 for the case of a square section. The corners of the section are labeled from 1 to n(in this case $n = 4$). Each one of them is removed step by step. The Karman-Trefftz transformation

$$z_{i+1} = \frac{1 + [(z_i - q_i)/z_i]^{\beta_i}}{1 - [(z_i - q_i)/z_i]^{\beta_i}} \tag{4.37}$$

is applied successively to the square section with i corners removed. Here, z_{i+1} is the plane containing the section with i corners removed, β_i is given by

$$\beta_i = \frac{\pi}{2 - \alpha_i} \tag{4.38}$$

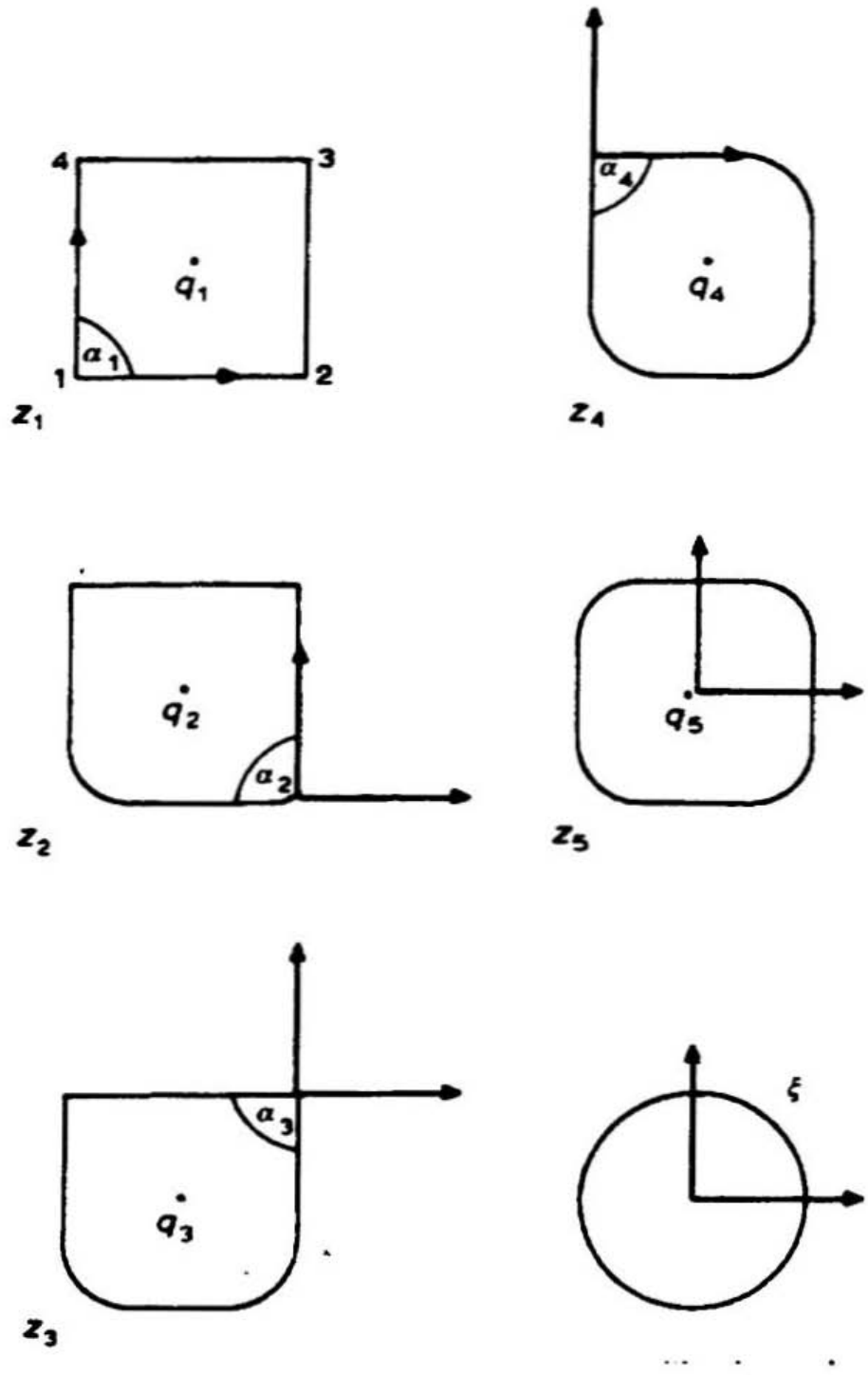

Figure 4.20: Karman-Trefftz, Theodorsen-Garrick transformations for a square[34].

and q_i is a point inside the section in the complex z_i plane. Here, q_i is the approximate centroid. The point q_{n+1} also forms the origin of the z_{n+1} plane. The origin of the complex plane z_i is taken to be the ith sharp corner at which the included angle is given by α_i. Once the sharp corners are removed, we are left with a rounded square or a near circle. This is mapped onto a unit circle via the Theodorsen-Garrick transformation. This is given by

$$z_{n+1} = \zeta exp\left[\sum_{j=0}^{M}(A_j + iB_j)\zeta^{-j}\right] \tag{4.39}$$

where the $2(M+1)$ coefficients in the above equation are found from the method of Ives using a fast Fourier transform technique which performs the required Fourier analysis and synthesis.

The first case of a body with sharp edges that was studied was the square cylinder. Shown in figure 4.21 is the mesh that was obtained in the physical plane.

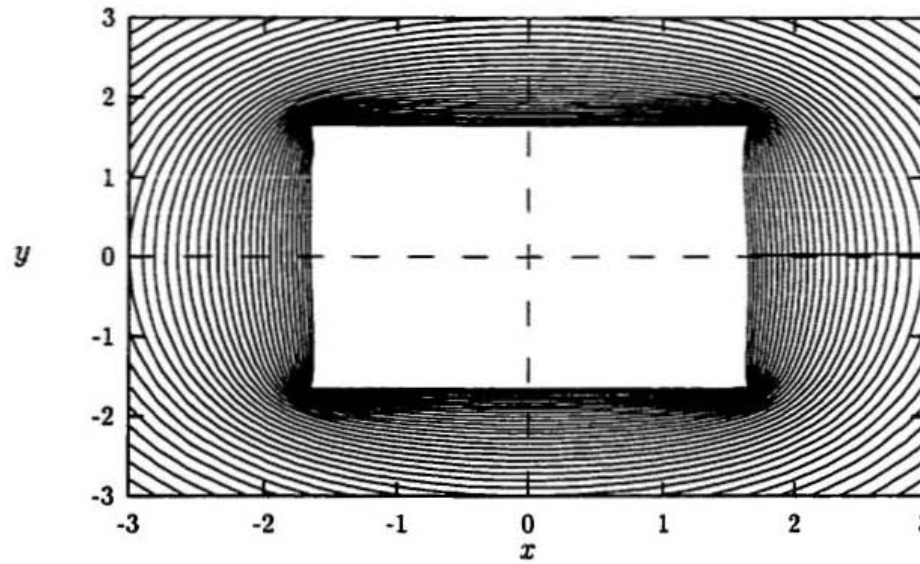

Figure 4.21: Mesh in the physical plane(square).

From the flow simulations carried out, plots of the drag coefficient and the mass coefficient were obtained. These are given in figure 4.22. Figure 4.23 shows the comparison of the force obtained using the above transformations and that obtained from Morison's equation at $C_D = 3.32$ and $C_M = 3.06$, at $KC = 2.42$, $\beta = 200$, and $\hat{\omega} = 1.571$.

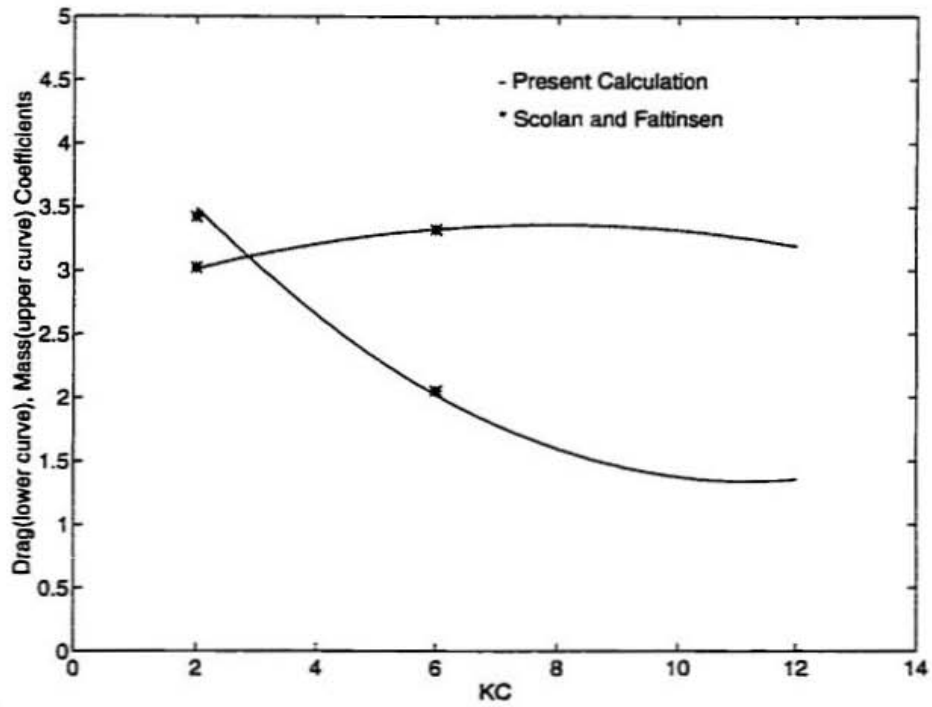

Figure 4.22: C_D, C_M *vs.* KC(square), $\beta = 200$

A fin was added to the square to simulate the effect of a skeg. The mesh in the physical plane is shown in figure 4.24. The respective results are shown in figures 4.25 and 4.26($C_D = 8.29$ and $C_M = 2.48$, at $KC = 1.65$, $\beta = 258$, and $\hat{\omega} = 1.571$).

Also shown below are the results of simulations carried out using a section of a boat with hard chines and a skeg. The comparison curves of F against t(figure 4.29

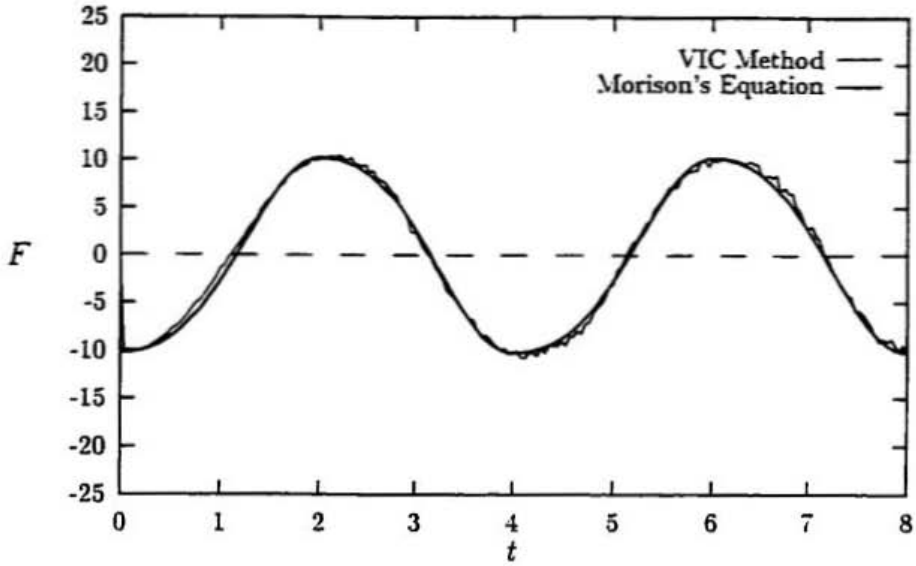

Figure 4.23: Fitting of $F(t)$ to Morison's equation(square).

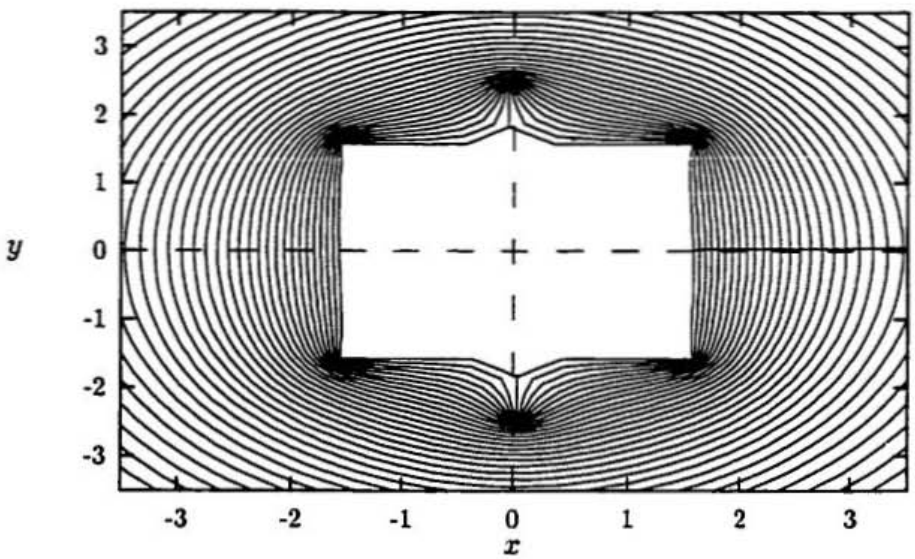

Figure 4.24: Mesh in the physical plane(square with a fin).

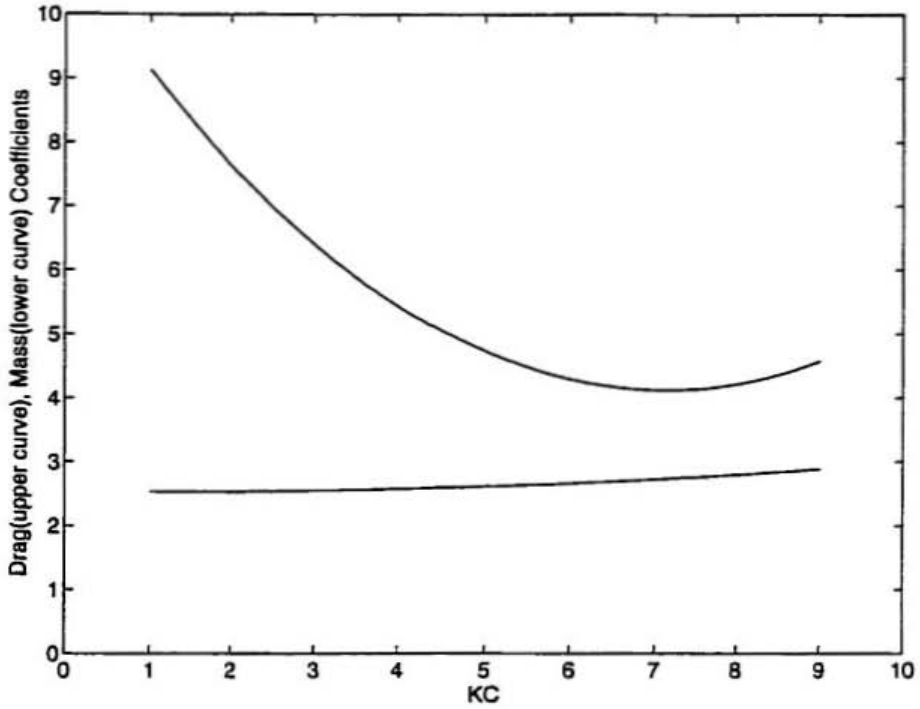

Figure 4.25: C_D, C_M *vs.* KC(square with a fin), $\beta = 258$, fin-length=0.78

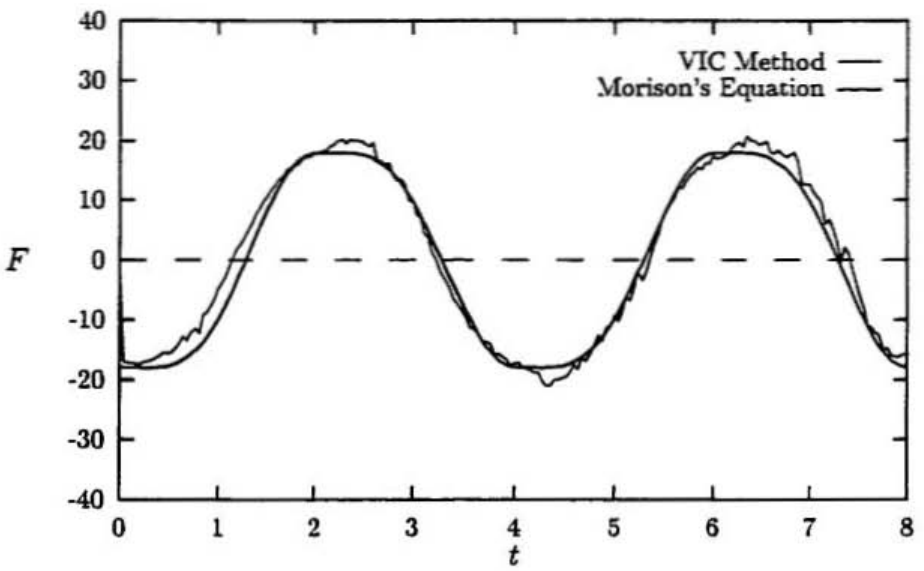

Figure 4.26: Fitting of $F(t)$ to Morison's equation(square with a fin).

were plotted for $C_D = 4.54$ and $C_M = 2.70$, at $KC = 2, 439$, and $\hat{\omega} = 1.11$.

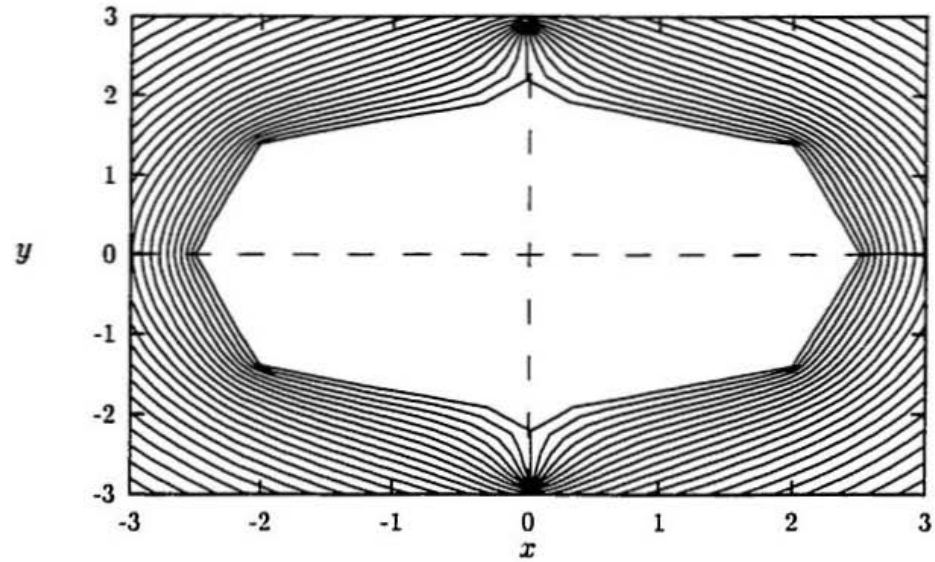

Figure 4.27: Mesh in the physical plane(boat section with a fin).

4.7 Discussion

The factors that affect the drag force are the size and strength of the shed vortices. These vortex properties are related to the size of the body, the velocity and frequency of the oscillatory flow and hence the Keulegan-Carpenter number, KC. The results for various flow simulations were obtained in the form of C_D and C_M against KC number curves and the fitting of $F(t)$ to Morison's equation. Shown also are the meshes in the physical planes that resulted from the transformation of the unit circle in the computational domain. Results for the circle in an oscillatory flow showed a very good agreement with the existing experimental values. A close agreement was also found between the results for a flat plate in cross oscillatory flow and a square with those obtained by Scolan and Faltinsen [32]. This provided

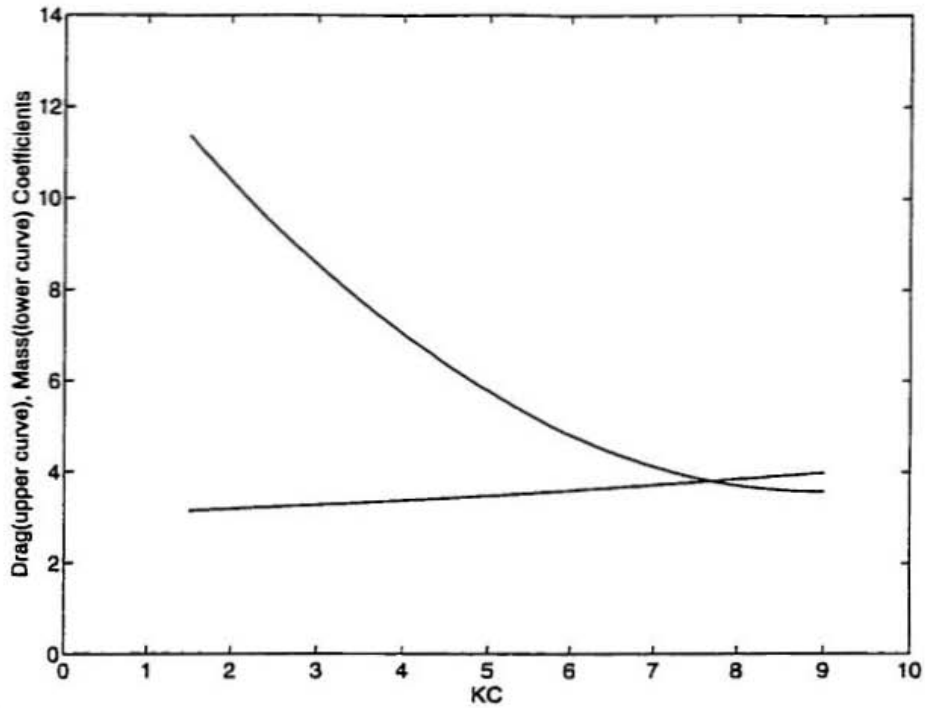

Figure 4.28: C_D, C_M *vs.* KC (boat section with a fin), $\beta = 439$, fin-length=0.82

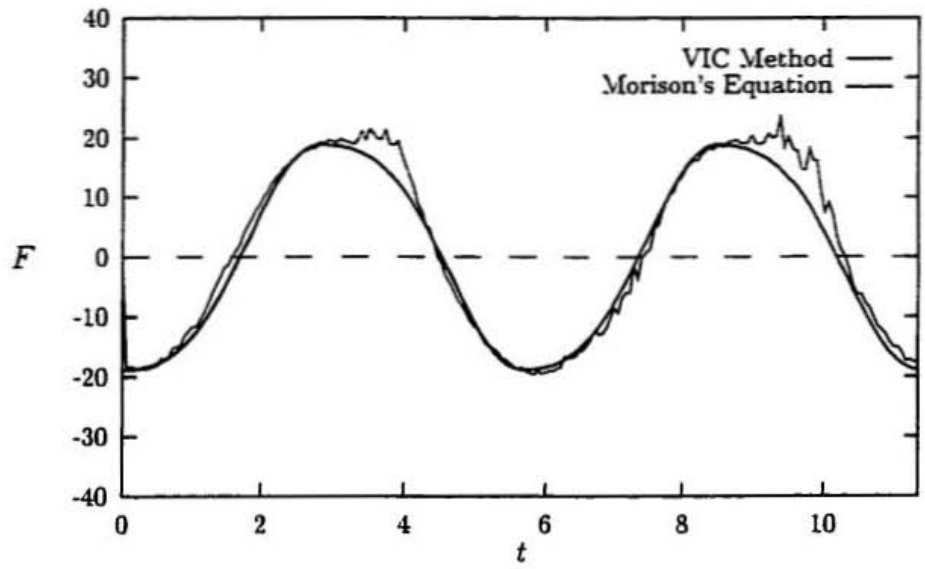

Figure 4.29: Fitting of $F(t)$ to Morison's equation(boat section with a fin).

us with a validation of the vortex-in-cell method when coupled with conformal mappings to study flows past bodies with other cross-sections.

Transformations, for a finned-cylinder, a rounded boat section, and sections with hard chines, were developed and applied to simulate flows past them. Similar values of C_D and C_M, at different KC numbers, were obtained for a finned-circle and the rounded boat section with a skeg. This was expected since the rounded boat section was nearly circular in shape. However, as would be expected, the values of C_D for the finned-circle were found to be higher than those for a circle, but the values of C_M were found to be lower than those for the circle. The curves of the non-dimensional drag force, $F(t)$, against time, t, also fitted well to the force curve generated by using the particular values of C_D and C_M in Morison's equation. The random component present was due to the random component present in the calculation procedure. In the case of sections with hard chines(sharp corners), the value of the truncation used was of the order of 0.1 and it is to be noted that the force coefficients varied considerably with the value of the truncation used. Determining the best way to establish the value of the truncation is a problem that needs further study.

Chapter 5

Conclusion

Some common vortex methods and the work done in the area of vortex- shedding due to flows past bluff bodies were reviewed. As a special case, a model based on the Point Vortex Method, following Clements [12], was constructed to simulate a two dimensional inviscid flow near the wake of a bluff body. Sample results were obtained in the form of the positions of the vortices at different instances of time and the rate of change of circulation with time. These were found to be in good comparison with those obtained by Clements himself. However, the model is based on inviscid flow and so it does not allow us to simulate the diffusion of vorticity in the flow nor does it accurately obtain the points of separation.

For viscous flows, another method, called the Vortex-In-Cell Method together with the Operator Splitting Technique of Chorin [23] was developed and used to carry out the flow simulations on a DEC 3000(Alpha microprocessor) computer. First, a steady flow past a circular cylinder was simulated and the results in the form of the time history of the drag force, the pressure and vorticity distribution on the cylinder surface, and the radial velocity on the x-axis behind the cylinder were obtained. These were found to be in a very good agreement with those of Stansby

and Smith [31]. Oscillatory flows past a circular-cylinder and bodies with other cross-sectional shapes were also simulated. To be able to calculate the viscous effects alone, assuming that the wave-making effects due to the free-surface can be determined separately, symmetry about the axis parallel to the direction of the flow was used. This converts the free-surface into a streamline and the flow to a symmetric flow about the x-axis past a body that is also symmetric about this axis. Results of each simulation were presented in the form of plots of the force coefficients, C_D and C_M, against the Keulegan-Carpenter number, KC, and the fitting of the time history of the drag force to Morison's equation. The calculated values of C_D and C_M for the cylinder, at different KC numbers showed excellent agreement with the existing experimental and numerical values.

Conformal mappings were used to study some non-circular sections numerically. As a result of the transformation, the appropriate modifications to the VIC method were made using the Jacobian of the transformation. Since this quantity vanishes at the sharp corners of the body, a treatment of the Jacobian was found to be necessary in the vicinity of the sharp edges to avoid numerical difficulties. This involved the truncation of the Jacobian to a finite value in the neighborhood of the corner. It was shown that the force coefficients calculated did not change much with the value of the truncation used in the case of the finned-circle. The values of C_D and C_M for the flat plate were also calculated and found to be in agreement with those determined by Scolan and Faltinsen [32]. Flows were also simulated past boat-sections of two types. For rounded sections, a conformal mapping that was numerically determined was used to transform a unit circle to the boat-section. To generate a section with a skeg, the unit circle was first mapped onto a unit circle with a fin via an elongated flat plate. The other type of boat-section studied was

one with hard chines. For such sections, the Karman-Trefftz transformation was first applied to remove the sharp corners and the resulting near-circle was then transformed to a unit circle using the Theodorsen-Garrick transformation. The results for the square were found to be very close to those of Scolan and Faltinsen. Force coefficients were also predicted for the section of a boat with hard chines and a skeg. Due to the lack of any experimental results for such a section, they were not verifiable.

All such numerical simulations involve a great deal of computations and hence CPU time. Owing to the numerous variables that affect the flow simulation, it becomes increasingly time consuming to try and study the effect of each in order to obtain as accurate results as possible. Due to such limitations, only the horizontal oscillatory flow past some relevant body sections was studied. This helped in predicting the swaying forces only. However, it is possible to simulate other motions such as the roll motion of a ship by changing some of the boundary conditions. Care must be taken to take into consideration the fact that the shape of the body changes with respect to the rigid free-surface. Also, in order to be able to try the various combinations of input variables, we should look for better(faster) solvers for equations, such as the Poisson's equation for the stream function, to cut down the computational time. Better simulation algorithms could also be developed to lower the computational effort by coming up with other techniques to reduce the number of computational elements to be tracked.

The Vortex-In-Cell Method when coupled with the conformal mapping technique enables us to simulate flows and predict the forces on a body with a cross-sectional shape that can be generated from a unit circle. Some common body-sections and some that are important to us in the area of Naval Architecture were

studied. It is possible to simulate flows past other cross-sections, like that of a cylinder with a multiple number of fins. etc.. and predict the forces and moments. This could help in the design process and improving on the shape of the sections of a moving craft, for instance, and cutting down on unwanted motions.

References

[1] Brown, D.T. and Patel M.H., "A theory for vortex shedding from the keels of marine vehicles", *Journal of Engineering Mathematics 19*, 1985, pp. 265-295.

[2] Rosenhead, L., "The Formation of Vortices from a Surface of Discontinuity", *Proceedings of the Royal Society, London*, A, Vol. 134, 1931, pp.170-192.

[3] Birkhoff, G. and Fisher, J., "Do Vortex Sheets Roll Up", *Circolo Mathematico Di Palermo Rendiconti*, Tomos 8, Series 2, 1959, pp. 77-89.

[4] Hama, F.R. and Burke, E.R, "On the Rolling-Up of a Vortex Sheet", *TN 6-1069*, Sept. 1960, U.S. Air Force Office of Scientific Research.

[5] Abernathy, F.H. and Kronauer, R.E., "The Formation of Vortex Sheets", *Journal of Fluid Mechanics*, Vol.13, Part 1, May 1962, pp. 1-20.

[6] Michalke, Von A., "Zur Instabilitat und nichtlinearen Entwicklung einergestorten Scherschicht", *Ingenieur-Archiv*, 33. Band, 4.Heft, 1964, pp. 264-276.

[7] Anton, L., "Ausbildung eines Wirbels an der Kante einer Platte", Gottinger Dissertation, *Ingenieur-Archiv*, Band 10, 1939, pp. 411-421.

[8] Kaden, H., *Ingenieur-Archiv*, Band II, 1931, pp.140-168.

[9] Wedemeyer, E., "Ausbildung eines Wirbelpaares an den Kanten einer Platte", *Ingenieur-Archiv*, Band 30, 1961, pp. 187-200.

[10] Blendermann, W., "Der Sprial-wirbel an translatorisch bewegten Kreeisbigenprofil; Struktur, Bewegung und Reaktion", *Schiffstechnik*, Band 16, Heft 80, Feb. 1969, pp. 3-13.

[11] Giesing, J.P., "Vorticity and Kutta Condition for Unsteady Multienergy Flows", *Transactions of the ASME, Series E. Journal of Applied Mechanics*, Vol. 36, No. 3, Sept. 1969, pp. 608-613.

[12] Clements, R.R., "An Inviscid Model of Two-Dimensional Vortex Shedding", *Journal of Applied Mechanics*, Vol. 57, Part 2, Feb. 1973, pp. 321-336.

[13] Gerrard, J.H., "Numerical Computation of the Magnitude and Frequency of the Lift on a Circular Cylinder", *Philosophical Transactions of the Royal Society*, Vol. 261, Jan. 1967, pp. 137-162.

[14] Brown, C.E. and Michael, W.H. Jr., "Effect of Leading-Edge Separation on the Lift of a Delta Wing", *NACA TN-3430*, April 1955.

[15] Smith, J.H.B., "Improved Calculations of Leading-Edge Separation from Slender, Thin, Delta Wings", *Proceedings of the Royal Society*, Series A, Vol. 306, 1968, pp. 67-90.

[16] Sack, A.H., Lundberg, R.E., and Hanson, C.W., "A Theoretical Investigation of the Aerodynamics of Slender Wing-Body Combinations Exhibiting Leading-Edge Separation", *NASA CR-719*, 1967.

[17] Hennig, G., "Ebene Umstromung von Querschnitten mit Wirbelpaar und Querkraftverteilung infolge Schraganstromung an Korpern mit kleinem Seitenverhaltnis", *Schiffbauforschung*, Band 9, 1970, pp. 229-245.

[18] Fuwa, T., "Hydrodynamic Forces Acting on a Ship in Oblique Towing", *Autumn Meeting, Society of Naval Architects of Japan*, November 1973. Preprint, pp. 161-173.

[19] Tatinclaux, J.C., "Experimental Investigation of the Drag Induced by Bilge Vortices", *Schiffstechnik*, Vol. 17, No. 87, May 1970, pp. 37-44.

[20] Soh, W.K. and Fink, P.T., "On Potential Flow Modeling of Action of Ships' Bilge Keels", *Proceedings of Fourth Australasian Conference on Hydraulics and Fluid Mechanics*, Monash University, Melbourne, Australia, December 1971, pp. 266-271.

[21] Hald, O.H. and Del Prete, V.M., *Math. Comput.* 32, 1978, pp. 791-809.

[22] Chorin, A.J., "Numerical Study of Slightly Viscous Flows", *Journal of Fluid Mechanics*, 57, 1973, pp. 785-796.

[23] Chorin, A.J., "Vortex Sheet Approximation of Boundary Layers", *Journal of Computational Physics*, 27, 1978, pp.428-442.

[24] Greengrad, Claude, "The Core Spreading Vortex Method Approximates the Wrong Equation", *Journal of Computational Physics*, 61, 1985, pp. 345-348.

[25] Yeung, Ronald W., Sphaier, Sergio H., and Vaidhyanathan, M., "Unsteady Separated Flow Around Blunt Bodies", *Proceedings of the Second International Offshore and Polar Engineering Conference*, San Francisco, USA, 1992, pp. 194-202.

[26] Carrier, J., Greengrad, L., Rokhlin, V., "A Fast Adaptive Multipole Algorithm for Particle Simulations", *SIAM J. Sci. Stat. Comput.*, Vol. 9, 1988, pp. 669-686.

[27] Christiansen, J.P., "Vortex Methods for Flow Simulation", *Journal of Computational Physics*, 13, 1973, pp. 363-379.

[28] Baker, G.R., *Journal of Computational Physics*, 31, 1979, pp. 76-95.

[29] Hockney, R.W., Goel, S.P., and Eastwood, J.W., *Journal of Computational Physics*, 14, 1974, pp. 148-158.

[30] Quartepelle, L. and Napolitano, M., "Force and Moment in Incompressible Flows", *AIAA Journal*, 21, 1983.

[31] Smith, P.A. and Stansby, P.K., "Impulsively Started Flow Around a Circular Cylinder by the Vortex Method", *Journal of Fluid Mechanics*, Vol. 194, 1988, pp. 45-77.

[32] Scolan, Y.M. and Faltinsen, O.M., "Numerical Studies Of Separated Flow From Bodies With Sharp Corners By The Vortex In Cell Method", *Journal of Fluids and Structures*, 1994, pp. 201-230.

[33] Ives, David C., "A Modern Look at Conformal Mapping Including Multiply Connected Regions". *AIAA Journal*, Vol. 14, No. 8, August 1976, pp. 1006-1011.

[34] Smith, P.A. and Stansby, P.K., "Viscous Oscillatory Flows Around Cylindrical Bodies At Low Keulegan-Carpenter Numbers Using The Vortex Method". *Journal of Fluid Mechanics*, Vol. 5, 1991, pp. 339-361.

[35] Macagno, Matilde, "A Comparison of Three Methods for Computing the Added Mass of Ship sections". *IIHR Report No. 104*, Iowa Institute of Hydraulic Research, April 1967.